



# Defect-engineered FeSe<sub>2-x</sub>@C with porous architecture for enhanced peroxymonosulfate-based advanced oxidation processes

Qiang Zhong<sup>a</sup>, Chenmin Xu<sup>a</sup>, Yazhi Liu<sup>a</sup>, Qiuyi Ji<sup>a</sup>, Zhe Xu<sup>a</sup>, Dunyu Sun<sup>a</sup>, Shuohua Zhou<sup>a</sup>, Bing Yang<sup>a</sup>, Yin hao Dai<sup>a</sup>, Chengdu Qi<sup>a</sup>, Shaogui Yang<sup>a,\*</sup>, Huan He<sup>a</sup>, Shiyin Li<sup>a</sup>, Cheng Sun<sup>b</sup>

<sup>a</sup> School of Environment, Nanjing Normal University, Nanjing, Jiangsu 210023, China

<sup>b</sup> State Key Laboratory of Pollution Control and Resource Reuse, School of the Environment, Nanjing University, Nanjing, Jiangsu 210023, China

## ARTICLE INFO

### Keywords:

Iohexol  
Defect-engineered  
Peroxymonosulfate  
Advanced oxidation processes  
Porous FeSe<sub>2-x</sub>@C

## ABSTRACT

A novel heterogeneous and porous FeSe<sub>2-x</sub>@C-5 with abundant Se vacancies ( $V_{Se}$ ) was facilely synthesized via one-step carbonization-selenization approach from Fe-MOFs (metal-organic frameworks) and firstly applied in activating peroxymonosulfate (PMS) for iohexol (IOH) removal, exhibiting extraordinary catalytic performance with superior stability and adaptability. The roles and functions of  $V_{Se}$  in the reaction system are deeply elucidated. Strikingly, systematic characterization and theoretical calculations revealed that  $V_{Se}$  can modulate the surface electronic structure and accelerate Fe<sup>3+</sup>/Fe<sup>2+</sup> cycle, leading to the strengthened binding energy and accelerated charge deliver for PMS activation. Accordingly, Iohexol (15 mg/L) can be eliminated within 30 min in FeSe<sub>2-x</sub>@C-5/PMS system, with apparent reaction rate constant ( $k_{app}$ ) 23.7 times higher than that in FeSe<sub>2</sub>/PMS system. This study not only contributes to a tutorial guideline for designing high-performance catalysts by virtue of structural control and  $V_{Se}$  engineering, but also extends its potential application in low-strength wastewater treatment.

## 1. Introduction

Iodinated X-ray contrast media (ICM), as a class of pharmaceutical and personal care products (PPCPs), is widely applied in medical diagnostic tests for X-ray imaging [1,2]. Iohexol (IOH) is a typical representative of ICM, which has been detected frequently in various water environments and wastewater treatment plant effluent in many cities around the world due to its persistent structure and high hydrophilicity [3–7]. Moreover, IOH may not only induce kidney toxicity and affect the thyroid homeostasis of organisms [8,9], but also generate disinfection by-products with high genotoxicity and cytotoxicity on cells [10,11]. In short, the existence of IOH in raw water induces a potential health risk. Therefore, it is urgent to develop effective approaches for in-depth degradation of subaqueous IOH.

To cope with the above challenges, plenty of technologies such as ozone oxidation [11], photocatalysis [12,13], ultraviolet oxidation [14], and biodegradation [15] etc., have been investigated in ICM degradation. However, these technologies have exhibited several disadvantages, such as insufficient efficiency, high energy consumption, harsh conditions and so on. Sulfate radical (SO<sub>4</sub><sup>•-</sup>) based advanced oxidation

processes (SR-AOPs) via activation of peroxymonosulfate (PMS) have attracted immense research interest owing to their higher oxidative potential (2.5–3.1 eV), long-lifetime ( $>3 \times 10^{-5}$  s), broader pH application range, and higher mineralization rate [16,17]. Therefore, these features of SO<sub>4</sub><sup>•-</sup> provide SR-AOPs promising application prospects for removing various refractory contaminants in water environment [12,18]. Various transition metal ions (Mn<sup>2+</sup>, Fe<sup>2+</sup>, Co<sup>2+</sup>, and Cu<sup>2+</sup>, etc.) have been investigated to activate PMS due to their facile operation, low energy consumption, and outstanding catalytic efficiency [19–21]. Specifically, Fe<sup>2+</sup> is considered to be one of the most promising transition metal ions with low cost, low biotoxicity, abundant existence, and high redox activity [22,23]. Nevertheless, the unavoidable secondary contamination and generation of iron-rich sludge restrict the application of homogeneous Fe<sup>2+</sup>/PMS system for pollutant degradation [22,24,25]. Hence, the development of Fe-based heterogeneous activator is strongly desirable. As a prospective nanomaterial, FeSe<sub>2</sub> has been widely explored for application in electrochemical energy storage, exhibiting excellent oxygen reduction activity and durability [26,27]. Nevertheless, the reports of FeSe<sub>2</sub> in activation of PMS for pollutant removal are rare. Recently, only Fang et al. have confirmed that nano-FeSe<sub>2</sub> can

\* Corresponding author.

E-mail address: [yangsg@njnu.edu.cn](mailto:yangsg@njnu.edu.cn) (S. Yang).

<https://doi.org/10.1016/j.apcatb.2022.121259>

Received 26 November 2021; Received in revised form 23 February 2022; Accepted 24 February 2022

Available online 26 February 2022

0926-3373/© 2022 Elsevier B.V. All rights reserved.

effectively activate PMS to degrade organic pollutants [28]. However, nano-scale catalyst is easy to agglomerate. In addition, the low  $\text{Fe}^{3+}/\text{Fe}^{2+}$  cycle efficiency and inadequate active sites from the under-developed structures restricted the actual application of nano- $\text{FeSe}_2$  in SR-AOPs. Therefore, the further construction of  $\text{FeSe}_2$ -based catalysts with fluent electron delivers, rich catalytic sites, and suitable electronic structure remains a challenge.

Metal organic frameworks (MOFs) are a class of marvelous crystalline materials with high porosity and surface area [29,30], which can also be treated as a superior material precursor for preparation of transition metal derivatives with well-defined porous structure via a pyrolysis method [26,31]. As a result, metal compounds can be wrapped in porous carbon nanocages, which can significantly prevent the leaching of metal ions [32]. More importantly, well-developed pores within metal compound@porous carbon compounds could not only facilitate the effective diffusion of molecules but also provide easier accessibility of active sites [33]. Therefore, Fe-based catalyst@porous carbon compounds derived from Fe-based metal organic frameworks (Fe-MOFs) have been extensively researched in the environmental field with optimistic application prospects [34–36]. Notwithstanding the progress already made,  $\text{FeSe}_2$ @porous carbon compounds derived from Fe-MOFs via a one-step carbonization–selenization is scarcely explored in the area of SR-AOPs until now.

Moreover, the geometric and electronic structure modulation are excellent methods for tuning the catalytic property of catalysts by subtly regulating the interfacial electronic coupling (e.g., optimal adsorption energies and electron deliver) between the catalyst surface and reaction intermediates [33,37]. Defect engineering, especially the introduction of surface vacancy engineering, is considered as an effective strategy to adjust the electronic configuration and the adsorption energy of reaction intermediate species [33,34,37]. Recently, it has been reported that oxygen vacancies can lower the reaction energy barrier [38], elongate the O–O bond of peroxide [20], accelerate interfacial electron transfer [33] and give rise to electron-rich unsaturated metal sites to promote Fenton-like reaction [37]. Similarly, Se vacancies ( $V_{\text{Se}}$ ) is one of the typical vacancy engineering with physicochemical properties similar to oxygen vacancies, which has been adopted frequently as an effective strategy for tuning intrinsic oxygen evolution electrocatalysts (OER) or hydrogen evolution reaction (HER) activity in electrocatalysts [26,39]. However, there are still no reports on the introduction of  $V_{\text{Se}}$  in  $\text{FeSe}_2$ -based catalysts and its application in SR-AOPs. Furthermore, the roles and functions of  $V_{\text{Se}}$  in SR-AOPs reactions mediated by  $\text{FeSe}_2$ -based compounds remain unclear.

Based on the above discussions, a series of defect-engineered  $V_{\text{Se}}$ -rich  $\text{FeSe}_{2-x}\text{@C}$  was constructed from Fe-MOFs via one-step carbonization and selenization process, which was used to promote PMS activation for degradation of recalcitrant organic compounds. The physicochemical properties of as-prepared catalyst were characterized in detail. Besides, the catalytic property of as-synthesized was assessed by activating PMS for IOH removal. The application prospects (reusability and stability) of the catalyst were also explored. Additionally, free radical capture experiments, electrochemical test, and electron paramagnetic resonance (EPR) were employed to determine active species. More importantly, the experimental characterizations, electrochemical test, and theoretical computations were combined to disclose the specific effect and superiority of  $V_{\text{Se}}$  during the SR-AOPs. Finally, frontier electron density (FED) simulations and liquid chromatography mass spectrometer (LC-MS) analysis were used to probe a possible IOH degradation pathway.

## 2. Experimental section

### 2.1. Materials

The detailed materials are presented in Text S1 of the Supporting Information (SI).

### 2.2. Preparation of Fe-MOFs, $\text{FeSe}_{2-x}\text{@C}$ , $\text{C}_{\text{MOFs}}$ and $\text{FeSe}_2$

Fe-MOFs was synthesized via a simple solvothermal method in the light of the previous reports proceeded with a modification [34]. Briefly, a certain amount of  $\text{FeCl}_3 \cdot 6\text{H}_2\text{O}$  (0.8 g), terephthalic acid (TA) (0.3 g) were dispersed in N, N-Dimethylformamide (DMF) (30 mL) and stirred for 30 min to form a homogeneous mixture. Subsequently, the resulting mixture was transferred to a 50 mL autoclave and kept for 24 h at 110 °C. After cooling down naturally, the product of Fe-MOFs was obtained by washing (with DMF and acetone) and vacuum drying at 80 °C overnight.

To prepare  $\text{FeSe}_{2-x}\text{@C}$ , the as-obtained Fe-MOFs (0.1 g) and Se powder (0.2 g) were uniformly mixed and transferred into a porcelain boat. Then, the porcelain boat was pre-treated to 350 °C at a heating rate of (2 °C min<sup>−1</sup>, 5 °C min<sup>−1</sup>, or 8 °C min<sup>−1</sup>) and maintained for 1 h in tube furnace, followed by the temperature rise from 350 °C to 450 °C at a heating rate of (2 °C min<sup>−1</sup>, 5 °C min<sup>−1</sup>, or 8 °C min<sup>−1</sup>) and maintained for 2 h in argon atmosphere. Finally, the  $\text{FeSe}_{2-x}\text{@C}$  powder was obtained after tube furnace cooling down to room temperature. According to the heating rate, the prepared composites were labeled as  $\text{FeSe}_{2-x}\text{@C-2}$ ,  $\text{FeSe}_{2-x}\text{@C-5}$ , and  $\text{FeSe}_{2-x}\text{@C-8}$ . The synthesis process of  $\text{FeSe}_{2-x}\text{@C}$  is shown in Scheme 1. For comparison, Text S2 of the SI gives the details for the preparation procedure of Fe-MOFs derived carbon (marked as  $\text{C}_{\text{MOFs}}$ ),  $\text{FeSe}_2$ , and physical mixing of  $\text{FeSe}_2$  and  $\text{C}_{\text{MOFs}}$  (marked as  $\text{FeSe}_2/\text{C}_{\text{MOFs}}$ ).

### 2.3. Characterization

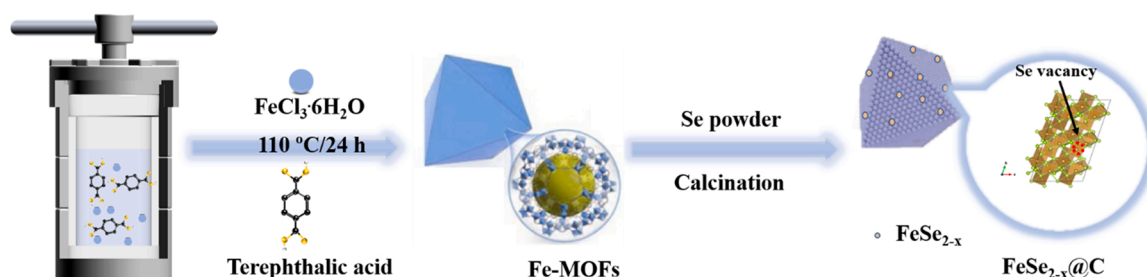
The X-ray diffraction (XRD, Rigaku Ultima III, Cu K $\alpha$  radiation) was conducted to identify the crystalline phase of as-synthesized samples. The surface morphologies and microstructure were explored by field emission scanning electron microscope (FE-SEM, JSM-7401 F, JEOL Ltd., Japan) and a high-resolution transmission electron microscope (HRTEM, JEM-2100 F, JEOL Ltd., Japan) with energy dispersive X-Ray spectroscopy (EDS). The chemical states and composition of samples were surveyed by X-ray photoelectron spectroscopy (XPS, ESCALAB Xi+, Thermo Fisher Scientific Ltd., USA). The functional group information of the sample was recorded by Fourier transform infrared spectra (FT-IR, Nicolet IS5, Thermo, USA). *In-situ* Raman was carried out on an HR Evolution Raman spectrophotometer (HORIBA Scientific Inc.), which was equipped with an Ar laser (532 nm, 180 Mw) as an excitation light source. The free radical and  $V_{\text{Se}}$  signals were detected by electron paramagnetic resonance (EPR, EMX-8, Bruker A300., Germany). Zeta potential measurements of samples were tested by Zetasizer Nano ZSE instrument.  $\text{N}_2$  adsorption-desorption isotherms were obtained using a Micrometrics ASAP 2460 system at −196 °C. The specific surface areas were calculated by the Brunauer–Emmett–Teller (BET) in a relative pressure ranging from 0.04 to 0.3. The ion concentrations ( $\text{Cl}^-$ ,  $\text{NO}_3^-$ ,  $\text{CO}_3^{2-}$ ,  $\text{PO}_4^{3-}$  and  $\text{SO}_4^{2-}$ ) for the actual water sample, Fe and Se released during the reaction were tested by an ion chromatography (ICS-1100, Thermo, USA) and an inductively coupled plasma-mass spectrometry (ICP-MS, NexION300X, PerkinElmer, USA). In addition, the detailed electrochemical test methods were given in Text S3 of SI.

### 2.4. Theoretical calculations details

The detailed calculation methods were given in Text S4 of SI.

### 2.5. Evaluation of catalytic performance

All experiments were executed in 50 mL beakers at room temperature of  $22 \pm 1$  °C unless otherwise stated. Firstly, certain amount of prepared catalyst sample was ultrasonically dispersed in the 50 mL IOH solution and constantly stirred for 20 min to reach the adsorption-desorption equilibrium. Then, certain amount of PMS was immediately added, and the pH of the reaction solution was not adjusted arti-



**Scheme 1.** Schematic illustration for the synthetic processes of the  $\text{FeSe}_{2-x}\text{@C}$  sample.

ficially which fluctuated within the range of 2.8–3.1 in most cases due to the presence of PMS. Further, at pre-determined time intervals, 0.8 mL suspension was sampled and filtered by 0.22  $\mu\text{m}$  membranes to remove particles after 0.2 mL of methanol was added quickly to terminate the reaction from proceeding. Then, the residual IOH concentration was detected by a high-performance liquid chromatography (1290, Agilent Technologies, USA) with a Venusil XBP C18 column ( $3.9 \times 200$ , Agela Technologies Inc.). The mobile phase of 0.1% formic acid water solution/methanol (90/10, vol/vol) was employed at a flow rate of  $1.0 \text{ mL} \cdot \text{min}^{-1}$ . The detection wavelength for IOH was set as 254 nm. The identification of intermediates was performed using HPLC/MS (Thermo Scientific, US). The mobile phase was obtained by mixing different ratio of acetonitrile and formic acid water (gradient program shown in Fig. S1) at a flow rate of  $0.5 \text{ mL} \cdot \text{min}^{-1}$ . The total organic carbon (TOC) was detected by a Shimadzu TOC-VCPH analyzer. The reaction rate constant of IOH degradation was fitted using the pseudo-first-order model. The equation as followed Eq. (1):

$$-\ln(C/C_0) = k_{app} \cdot t \quad (1)$$

where  $C_0$  (mg/L) and  $C$  (mg/L) are the concentration of IOH at the original and different reaction time ( $t$  min), and  $k_{app}$  ( $\text{min}^{-1}$ ) is the apparent reaction rate constant. The concentration of  $\text{Fe}^{2+}$  was measured and the detailed test methods were given in Text S5 of SI.

### 3. Results and discussions

#### 3.1. Morphology and chemical structures

The surface morphologies and microstructures of the as-prepared Fe-MOFs,  $\text{FeSe}_2$ ,  $\text{FeSe}_{2-x}\text{@C-5}$  composites were investigated by FE-SEM and TEM (Fig. 1). As illustration of Fig. 1(a) and (b), Fe-MOFs unveiled a well-defined octahedron crystallization structure with particle sizes around  $\sim 500 \text{ nm}$ . Simultaneously, the XRD characteristic peaks were consistent with MIL-101(Fe) [40] (Fig. S2). After a one-step carbonization-selenization process (Fig. 1(c) and (d)), it could be unambiguously observed that  $\text{FeSe}_{2-x}\text{@C-5}$  still retained the pristine morphology of the MIL-101(Fe) after calcination. As expected, the as-derived  $\text{FeSe}_{2-x}\text{@C-5}$  consisted of small-scale  $\text{FeSe}_{2-x}$  nanoparticles which were uniformly confined in a porous carbon layer. Furthermore, plentiful pores and cracks were created on the surface of  $\text{FeSe}_{2-x}\text{@C-5}$ , which would reduce mass transfer resistance and expose more active sites to accelerate the SR-AOPs reaction [33,34]. The EDS mapping of  $\text{FeSe}_{2-x}\text{@C-5}$  (Fig. S3(a–d)) indicated the evenly distribution of Fe, Se, and C elements throughout the  $\text{FeSe}_{2-x}\text{@C-5}$  particles. The EDS elemental analysis (Fig. S3(e)) implied the mole ratio of Fe/Se at approximately 1/2, which was similar to the stoichiometric relationship of  $\text{FeSe}_2$  and further confirmed the successful formation of  $\text{FeSe}_{2-x}\text{@C-5}$ . The as-synthesized  $\text{FeSe}_2$  exhibited irregular morphology with

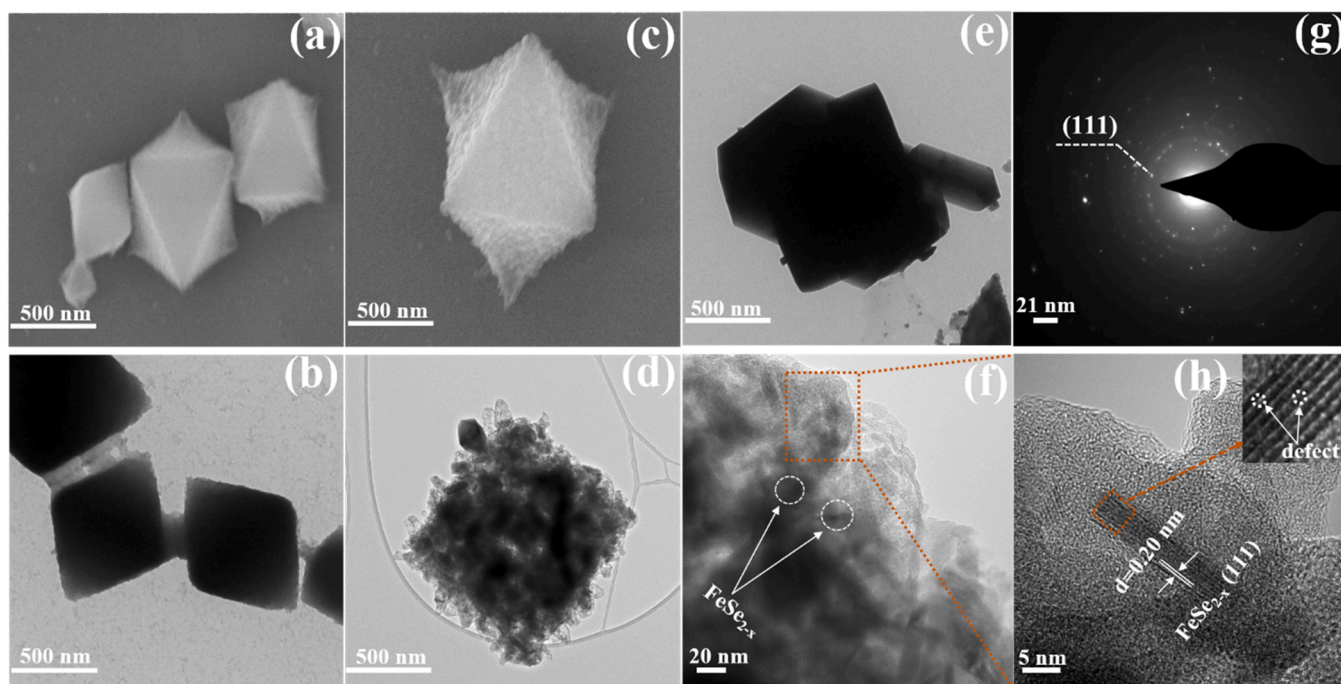


**Fig. 1.** (a) SEM image and (b) TEM image of Fe-MOFs; (c) SEM image and (d) TEM image for  $\text{FeSe}_{2-x}\text{@C-5}$ ; (e) TEM image of  $\text{FeSe}_2$ ; (f, h) HRTEM image and (g) FFT pattern for  $\text{FeSe}_{2-x}\text{@C-5}$ .



particle size around  $\sim 1.36 \mu\text{m}$  (Fig. 1(e)), which was much larger than that of  $\text{FeSe}_{2-x}@\text{C}-5$  (Fig. 1(f)). Fast Fourier transform (FFT) (Fig. 1(g)) pattern and HRTEM (Fig. 1(h)) image further confirm the presence of  $\text{FeSe}_{2-x}$  (111), which were consistent with the crystal facet distance of 0.20 nm. In addition, the inset in Fig. 1(h) suggested lattice fringes were sunken with certain degree of lattice defects, which might be attributed to the presence of  $V_{\text{Se}}$  [41]. And this phenomenon will be further confirmed via systematic characterization later. These characteristics surface defect engineering ( $V_{\text{Se}}$ ) can obviously influence the electronic state of catalysts, which endowed  $\text{FeSe}_{2-x}@\text{C}-5$  potential superiority as catalyst for pollutant removal. Theoretically, for a  $\text{FeSe}_2$  unit cell without defection, a Fe atom ligated six Se atoms to forming an octahedron, and each Se atom was connected with three Fe centers to become a tetrahedron [28]. Simultaneously, a theoretical model was also exhibited with rich  $V_{\text{Se}}$  of  $\text{FeSe}_{2-x}$  crystal (Fig. S4).

The crystalline structures of the as-synthesized samples were characterized using XRD (Figs. 2(a) and S5). It was observed that all the characteristic peaks for the four as-synthesized catalysts were well-defined and matched well with the standard card of orthorhombic ferroselite (JCPDS No: 74-0247) [42,43]. Compared to  $\text{FeSe}_2$ , the diffraction peak positions (strongest peaks at  $35.1^\circ$  corresponded to the (111) of  $\text{FeSe}_{2-x}@\text{C}-2$ ,  $\text{FeSe}_{2-x}@\text{C}-5$ , and  $\text{FeSe}_{2-x}@\text{C}-8$  shifted to lower angles and displayed a relatively poor crystallinity, indicating the appearance of surface  $V_{\text{Se}}$  [43,44]. Analogous conclusions were also acquired from the magnified FT-IR and Raman spectra. As depicted in magnified FT-IR (Fig. 2(b)), the characteristic absorption peaks at  $406.5 \text{ cm}^{-1}$  and  $417.6 \text{ cm}^{-1}$  were ascribed to the Fe–Se in  $\text{FeSe}_2$ . Compared to  $\text{FeSe}_2$ , it would be clearly observed the  $\text{FeSe}_{2-x}@\text{C}-2$ ,  $\text{FeSe}_{2-x}@\text{C}-5$ , and  $\text{FeSe}_{2-x}@\text{C}-8$  shifted negatively, which indicated the existence of surface  $V_{\text{Se}}$ . As illustrated in Fig. 2(c), the Raman spectra of  $\text{FeSe}_2$ ,  $\text{FeSe}_{2-x}@\text{C}-2$ ,  $\text{FeSe}_{2-x}@\text{C}-5$ , and  $\text{FeSe}_{2-x}@\text{C}-8$  samples all exhibited four strong distinctive vibrational bands at around  $180.3 \text{ cm}^{-1}$ ,  $217.6 \text{ cm}^{-1}$  ( $A_{1g}$ ),  $257.9 \text{ cm}^{-1}$  ( $B_{1g}$ ), and  $288.3 \text{ cm}^{-1}$ . Furthermore, the band in  $217.6 \text{ cm}^{-1}$ ,  $257.9 \text{ cm}^{-1}$  could be attributed to the modes of  $\nu_{\text{Se-Se}}$  vibrations [45]. Similarly, the strong characteristic peaks at  $180.3 \text{ cm}^{-1}$  and  $288.3 \text{ cm}^{-1}$  corresponded to the stretching

vibration of Se–Se and Fe–Se, respectively [46]. On one hand, the results suggested that the as-prepared catalysts were mainly composed of  $\text{FeSe}_2$ , which were in accordance with XRD results. On the other hand, compared to  $\text{FeSe}_2$ , the vibration peaks of  $\text{FeSe}_{2-x}@\text{C}-2$ ,  $\text{FeSe}_{2-x}@\text{C}-5$ , and  $\text{FeSe}_{2-x}@\text{C}-8$  red-shifted, and their full width at half-maximum values in Se–Se ( $180.3 \text{ cm}^{-1}$ ) decreased gradually, indicating that different concentrations of  $V_{\text{Se}}$  could be produced in the corresponding catalysts [47]. In addition, As shown in Fig. S6, Raman characteristic peaks both in D band ( $\sim 1530 \text{ cm}^{-1}$ ) and G band ( $\sim 1580 \text{ cm}^{-1}$ ) represented carbonaceous material (amorphous C and graphitic C) of  $\text{FeSe}_{2-x}@\text{C}-2$ ,  $\text{FeSe}_{2-x}@\text{C}-5$ , and  $\text{FeSe}_{2-x}@\text{C}-8$  [32]. Further, the defect degree of C was also assessed by the intensity of  $I_D/I_G$  values, and the  $\text{FeSe}_{2-x}@\text{C}-2$ ,  $\text{FeSe}_{2-x}@\text{C}-5$ , and  $\text{FeSe}_{2-x}@\text{C}-8$  exhibited a small and similar  $I_D/I_G$  values of 0.4528, 0.4479, and 0.4924 respectively, indicating that the pyrolysis temperature exhibited negligible influence on the generation of structural defects within the C structures.

The surface components and chemical states of as-prepared samples were obtained by XPS analysis. As revealed in Fig. S7, all of the as-prepared samples displayed characteristic peaks of Fe 2p, C 1s, Se 3d, and Se 3p, which was in conformity to the EDS analysis. Additionally, the presence of  $V_{\text{Se}}$  might alter the coordination of Se atoms and the Se contents [26]. The  $V_{\text{Se}}$  concentrations were further analyzed by Se 3d spectra (Fig. 2(e)). The deconvolution of Se 3d spectra for  $\text{FeSe}_{2-x}@\text{C}-5$  was at about 54.5, 55.7, and 56.6 eV, which could be assigned to Se  $3d_{5/2}$  ( $\text{Se}^{2-}$ ), Se  $3d_{5/2}$  ( $\text{Se}^{\cdot}$ ), and Se  $3d_{3/2}$  ( $\text{Se}^{\cdot}$ ), respectively [48]. The results were also consistent with the Raman and XRD analysis. More importantly, the peak intensity and area ratio of Se  $3d_{3/2}$  in  $\text{FeSe}_{2-x}@\text{C}-5$  was much lower than those in  $\text{FeSe}_2$ ,  $\text{FeSe}_{2-x}@\text{C}-2$ , and  $\text{FeSe}_{2-x}@\text{C}-8$ , suggesting the increase of low-coordination Se atoms with the presence of more  $V_{\text{Se}}$  [26]. Similarly, as shown in Table S1, the Se content has been significantly reduced after heat treatment, indicating that part of Se atoms have been removed and the  $V_{\text{Se}}$  have been formed in as-prepared catalyst. Meanwhile, the  $V_{\text{Se}}$  concentrations could be regulated by employing a "selenium extraction" through controlling the ramp rate of calcination ( $2^\circ\text{C min}^{-1}$ ,  $5^\circ\text{C min}^{-1}$ , or  $8^\circ\text{C min}^{-1}$ ). It was worth noting that the ramp rate at  $5^\circ\text{C min}^{-1}$  caused higher

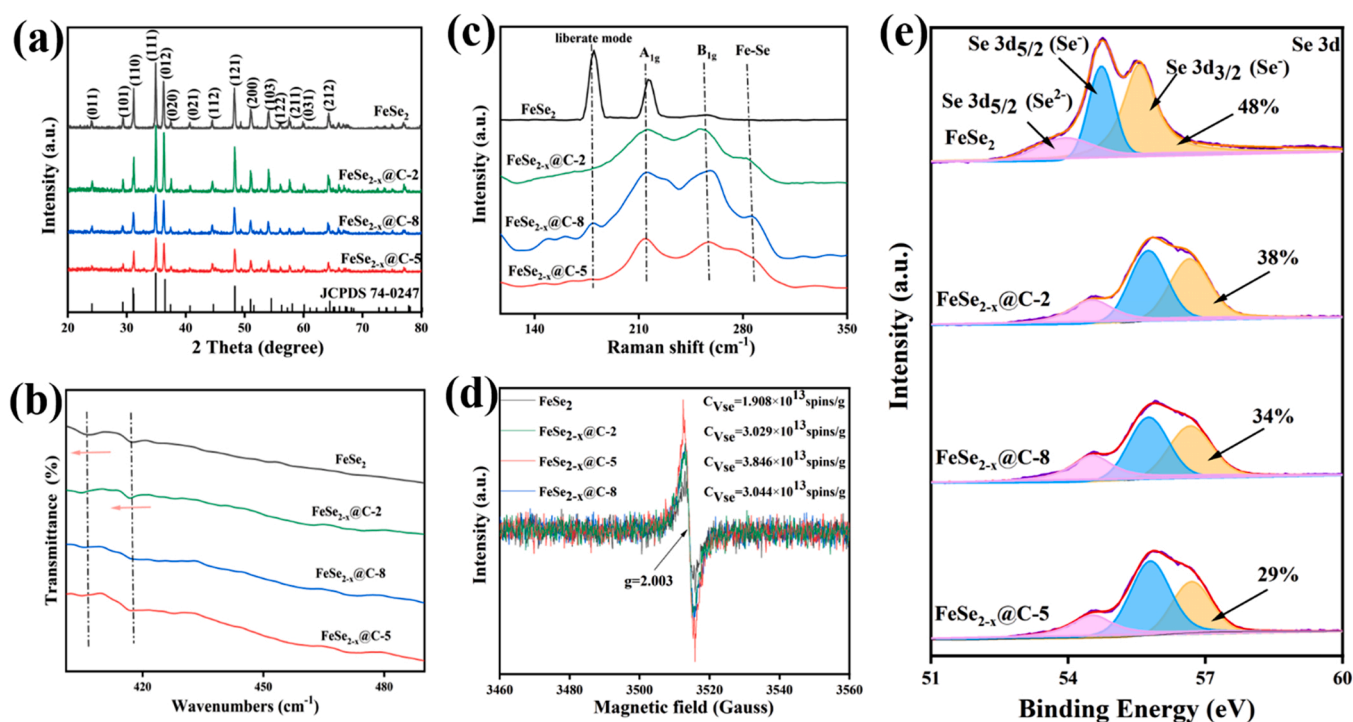


Fig. 2. (a) XRD pattern, (b) magnified FT-IR spectra, (c) Raman spectra, (d) EPR spectra and (e) XPS analysis of Se 3d for  $\text{FeSe}_2$ ,  $\text{FeSe}_{2-x}@\text{C}-2$ ,  $\text{FeSe}_{2-x}@\text{C}-5$ , and  $\text{FeSe}_{2-x}@\text{C}-8$ , respectively.



concentration of  $V_{se}$  on the catalyst surface. EPR was a powerful and effective technique to identify the presence and concentration of  $V_{se}$ . Therefore, similar results can be obtained from EPR patterns (Fig. 2(d)). Typically, a resonance single at  $g = 2.003$  represented the presence of  $V_{se}$  [49] and the concentration followed the order of  $FeSe_{2-x}@C-5$  ( $3.846 \times 10^{13}$  spins/g) >  $FeSe_{2-x}@C-8$  ( $3.044 \times 10^{13}$  spins/g) >  $FeSe_{2-x}@C-2$  ( $3.029 \times 10^{13}$  spins/g) >  $FeSe_2$  ( $1.908 \times 10^{13}$  spins/g). Therefore, catalysts with different concentrations of  $V_{se}$  have been favorably synthesized, which laid a strong bedrock for the further utilization of  $V_{se}$ -engineered to guide electron modulation of catalyst. Additionally, the strengthened EPR signals of  $FeSe_{2-x}@C-5$  were attributed to the electron-trapped centers at  $V_{se}$  defects, suggesting that a large number of single electrons in  $FeSe_{2-x}@C-5$  might be captured [26], and these electron pairs provided the surface of  $FeSe_{2-x}@C-5$  a certain degree of reducibility [50]. As a result, by introducing  $V_{se}$  into catalyst, the surface electronic structure and reducibility of catalysts can be significantly regulated, and ultimately affect the catalytic activity of the catalyst.

In addition, the Fe  $2p_{3/2}$  high-resolution spectra of as-prepared samples were also analyzed, as portrayed in Figs. 3(a) and S8. The characteristic peaks at binding energy (BE) of 706.9 belonged to  $Fe^{2+}$  of  $FeSe_2$ , while the minor and broad peak at about 710.0 eV can be ascribed to  $Fe^{2+}$  of iron oxide by the partial surface oxidation of  $FeSe_2$  nanospheres [28]. Besides, the vertices at BE of 711.4 eV were distinctive features of  $Fe^{3+}$ , satellite peaks (indicated by "Sat.") were also observed at 713.5 eV [34]. As depicted in Fig. 3(b), Fe 2p peaks of

$FeSe_{2-x}@C-2$ ,  $FeSe_{2-x}@C-5$ , and  $FeSe_{2-x}@C-8$  shifted to the lower binding energy in comparison with  $FeSe_2$  owing to the presence of  $V_{se}$ . It also proved that the existence of  $V_{se}$  is favorable to change chemical environment (electronic structure and ion coordination number) of Fe atoms owing to the modulation of Fe-Se bonds, which was in accordance with results of the  $V_{se}$ -rich  $Co_{0.85}Se_{1-x}$  as previous reported [26].

Afterwards, Zeta potential of as-prepared samples were investigated in neutral deionized water (pH = 7.82) (Fig. 3(c)). The Zeta potential values of the  $FeSe_2$ ,  $FeSe_{2-x}@C-2$ ,  $FeSe_{2-x}@C-5$ , and  $FeSe_{2-x}@C-8$  was  $-6.72$ ,  $-10.77$ ,  $-17.7$ , and  $-11.68$  mV, respectively. As far as our know, the formation of  $V_{se}$  results in the presence of lone pair electrons suggests the enrichment of electrons. Namely, the greater concentration of  $V_{se}$  is, the more negative Zeta potential of the samples will be [51]. Therefore, the results of Zeta potential indicated that  $FeSe_{2-x}@C-5$  owned the highest  $V_{se}$  concentration and  $FeSe_2$  possessed the lowest. The result matches well with EPR and XPS. Besides, the co-ordination of carbonaceous species remaining on the surface of the  $FeSe_{2-x}@C-5$  was also analyzed (Fig. S9), the C 1s spectra could also be fitted into two peaks at 284.8 and 287.8 eV, which were assigned to the C-C and O-C=O, respectively [52].

Moreover,  $N_2$  adsorption/desorption results and homologous pore size distribution of  $FeSe_2$ ,  $FeSe_{2-x}@C-2$ ,  $FeSe_{2-x}@C-5$  and  $FeSe_{2-x}@C-8$  were depicted in Figs. 3(d) and S10.  $FeSe_{2-x}@C-2$ ,  $FeSe_{2-x}@C-5$ , and  $FeSe_{2-x}@C-8$  displayed type IV isotherms and H3 hysteresis loops, which indicated the presence of hierarchical pores [53]. Furthermore,

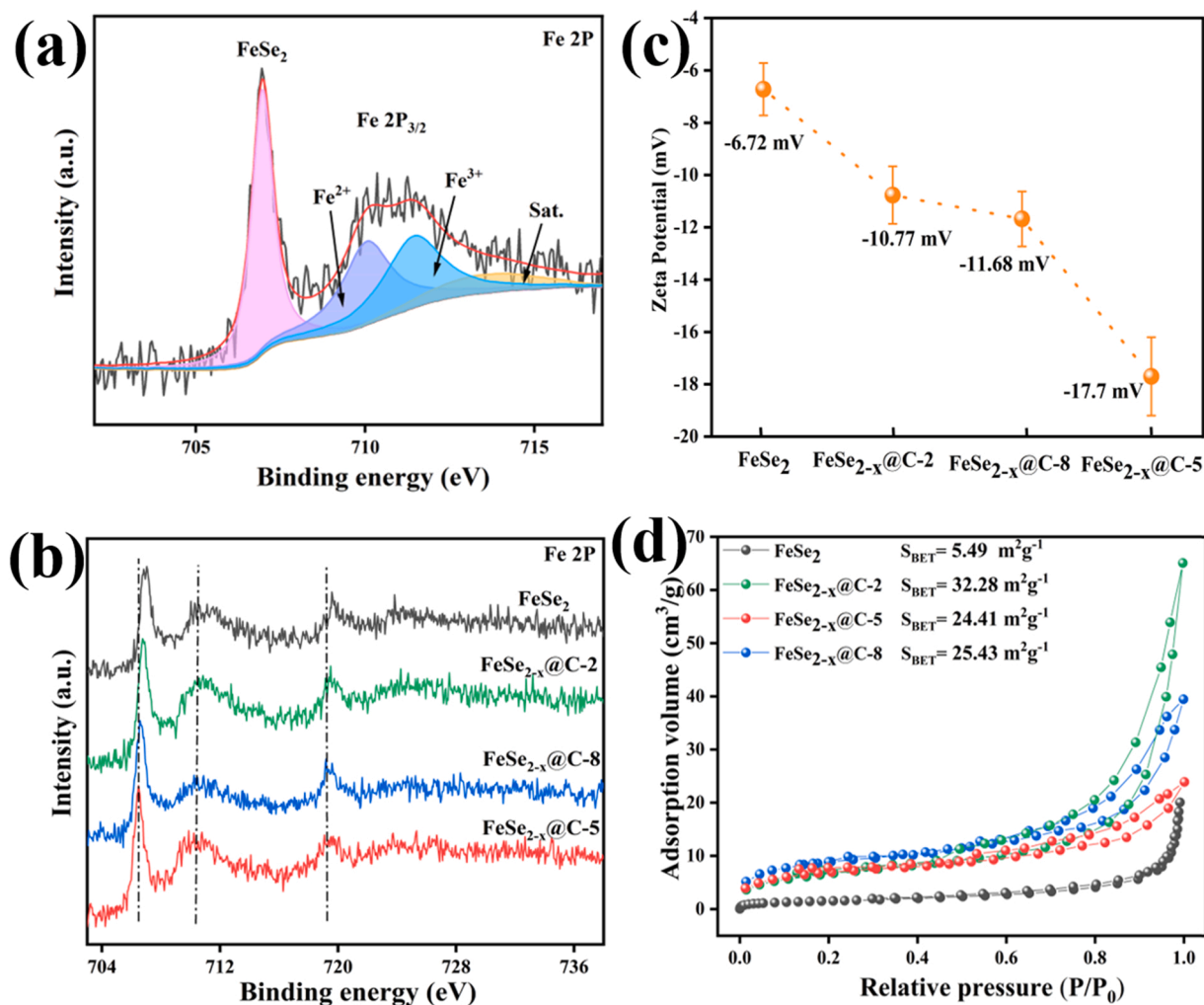


**Fig. 3.** (a) XPS analysis of Fe  $2p_{3/2}$  for  $FeSe_{2-x}@C-5$ , (b) XPS analysis of Fe 2p for  $FeSe_2$ ,  $FeSe_{2-x}@C-2$ ,  $FeSe_{2-x}@C-5$ , and  $FeSe_{2-x}@C-8$ , (c) Zeta potential and (d)  $N_2$  adsorption/desorption isotherms of  $FeSe_2$ ,  $FeSe_{2-x}@C-2$ ,  $FeSe_{2-x}@C-5$ , and  $FeSe_{2-x}@C-8$ , respectively.

the  $\text{FeSe}_2$  obtained by hydrothermal-calcination strategy showed an exceedingly low specific surface area ( $5.49 \text{ m}^2/\text{g}$ ) and small pore volume ( $0.030 \text{ cm}^3/\text{g}$ ), relative to those of  $\text{FeSe}_{2-x} @ \text{C}-2$ ,  $\text{FeSe}_{2-x} @ \text{C}-5$ , and  $\text{FeSe}_{2-x} @ \text{C}-8$  derived from Fe-MOFs precursors. These results indicated that the  $\text{FeSe}_{2-x} @ \text{C}-2$ ,  $\text{FeSe}_{2-x} @ \text{C}-5$ , and  $\text{FeSe}_{2-x} @ \text{C}-8$  prepared from Fe-MOFs as precursors demonstrated higher specific surface area ( $24.21 - 32.28 \text{ m}^2/\text{g}$ ) and plentiful micro- and mesopores construction (pore volume  $0.036 - 0.095 \text{ cm}^3/\text{g}$ ), which would increase the exposure of catalytic sites and improve mass transfer property for pollutant degradation.

### 3.2. Catalytic performance of $\text{FeSe}_2$ -based catalysts for IOH degradation

In order to evaluate catalyst activity and ascertain the effects of  $V_{\text{se}}$  contents on  $\text{FeSe}_2$ ,  $\text{FeSe}_{2-x} @ \text{C}-2$ ,  $\text{FeSe}_{2-x} @ \text{C}-5$ , and  $\text{FeSe}_{2-x} @ \text{C}-8$  catalytic activity for PMS activation, the degradation of IOH were carried out. Control degradation systems (Fe-MOFs/PMS,  $\text{C}_{\text{MOFs}}$ /PMS,  $\text{FeSe}_2/\text{C}_{\text{MOFs}}$ /PMS, PMS) were also executed under the same conditions. All the catalysts were stirred for 20 min in the aqueous solutions of IOH to reach adsorption-desorption equilibrium before addition of PMS. As depicted in Fig. 4(a), all catalysts exhibited an insignificant adsorption for IOH. Similarly, it could be seen that PMS without activation does not

induce obvious IOH degradation. After adding PMS, a weak removal of IOH might be initiated by the  $\text{C}_{\text{MOFs}}$  via non-radical mechanisms [54]. As for Fe-MOFs and  $\text{FeSe}_2$ , nearly 36.4% and 28.8% of IOH could be degraded respectively with the addition of PMS, indicating that Fe-MOFs and  $\text{FeSe}_2$  could not effectively activate PMS to generate active species. The simultaneous presence of PMS and  $\text{FeSe}_{2-x} @ \text{C}$  catalyst (one of the  $\text{FeSe}_{2-x} @ \text{C}-2$ ,  $\text{FeSe}_{2-x} @ \text{C}-5$ , and  $\text{FeSe}_{2-x} @ \text{C}-8$ , denoted as  $\text{FeSe}_{2-x} @ \text{C}-(2,5,8)$ ) led to a significantly increase in IOH removal efficiency compared with  $\text{FeSe}_2/\text{PMS}$  degradation systems. Interestingly, after physical mixing  $\text{FeSe}_2$  and  $\text{C}_{\text{MOFs}}$  to activate PMS, lower removal efficiency for  $\text{FeSe}_2/\text{C}_{\text{MOFs}}$  was observed compared with  $\text{FeSe}_{2-x} @ \text{C}-(2,5,8)/\text{PMS}$  system. These results suggested that the increased reactivity of  $\text{FeSe}_{2-x} @ \text{C}-(2,5,8)$  was probably related to the structural changes (e.g., structural defect) rather than the simple synergistic effect between  $\text{FeSe}_{2-x}$  and C species. Specifically,  $\text{FeSe}_{2-x} @ \text{C}-5$  presented the optimal catalytic performance and IOH can be completely removed within 30 min. In addition, it was also found that the degradation kinetics of IOH for all catalysts could be well fitted by the pseudo-first-order kinetic model (Fig. 4(b)). The apparent reaction rate constant ( $k_{\text{app}}$ ) in  $\text{FeSe}_{2-x} @ \text{C}-5$  was  $0.1328 \text{ min}^{-1}$ , much higher than that of  $\text{FeSe}_2$  ( $0.0056 \text{ min}^{-1}$ ),  $\text{FeSe}_{2-x} @ \text{C}-2$  ( $0.0451 \text{ min}^{-1}$ ), and  $\text{FeSe}_{2-x} @ \text{C}-8$  ( $0.0605 \text{ min}^{-1}$ ). The  $k_{\text{app}}$  of  $\text{FeSe}_{2-x} @ \text{C}-5$  is about 23.7 times higher than that of  $\text{FeSe}_2$ ,

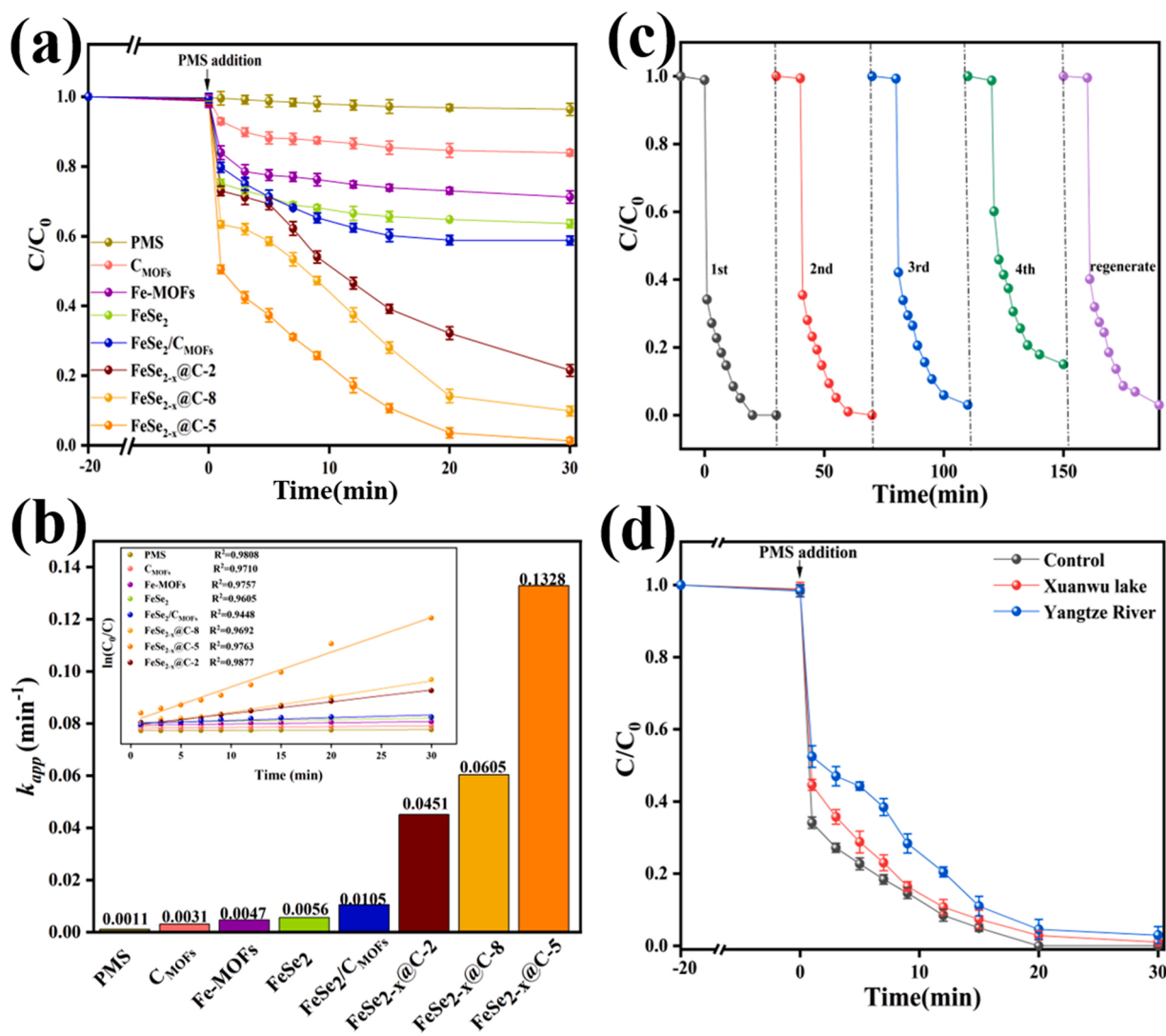


**Fig. 4.** (a) Catalytic degradation of IOH under different conditions and (b) the corresponding pseudo first-order kinetic analysis results. Reaction conditions:  $[\text{IOH}]_0 = 15.0 \text{ mg/L}$ ,  $[\text{PMS}]_0 = 1.0 \text{ mM}$ ,  $[\text{catalyst}]_0 = 0.2 \text{ g/L}$ . (c) The recyclability of  $\text{FeSe}_{2-x} @ \text{C}-5$  for IOH degradation. (d) Degradation of IOH in different water environment with  $\text{FeSe}_{2-x} @ \text{C}-5/\text{PMS}$ . Reaction conditions:  $[\text{IOH}]_0 = 15.0 \text{ mg/L}$ ,  $[\text{PMS}]_0 = 1.5 \text{ mM}$ ,  $[\text{catalyst}]_0 = 0.2 \text{ g/L}$ .

demonstrating that the porous  $\text{FeSe}_{2-x}$ @C-5 with more  $V_{\text{se}}$  sites exhibited higher catalytic performance. Additionally, it can be found that there is a positive correlation between the  $V_{\text{se}}$  and  $k_{\text{app}}$  from Fig. S11, that is to say, the catalytic activity of defect-engineered  $\text{FeSe}_{2-x}$ -based material for IOH degradation could be handily optimized via controlling the  $V_{\text{se}}$  contents. Moreover, the summary of ICM degradation by persulfate-based advanced oxidation is listed in Table S3. Compared with other studies,  $\text{FeSe}_{2-x}$ @C-5/PMS system has a shorter reaction time, higher efficiency and greater reaction rate constant for the degradation of ICM. Thus,  $\text{FeSe}_{2-x}$ @C-5/PMS system has the potential to eliminate ICM in aqueous solution with high efficiency.

In addition, to examine the stability and reusability of  $\text{FeSe}_{2-x}$ @C-5 catalyst during the catalytic reactions, cycling experiments were carried out under the same catalytic conditions. As shown in Figs. 4(c) and S12, the IOH degradation efficiency still reached 85.0% after four repetitive experiments. And the concentration of Fe and Se released during the repetitive experiments ranged from 0.6 to 1 mg/L and 0.002–0.009 mg/L, which met the class I standard of the integrated wastewater of Fe discharge standards (10 mg/L, GB 8978–2002, 174 Chinese Environmental Protection Agency) and the standard of the integrated wastewater of Se discharge standards (0.01 mg/L, GB5749–2006, Chinese Environmental Protection Agency), respectively. Interestingly, the above results indicated that Fe leaching is 300–500 times higher than Se leaching, and the existence form of residual Se species after most of Fe etching was discussed in detail in Text S6 of Support Information. Notably, repeated experiments demonstrated an outstanding stability and reusability of  $\text{FeSe}_{2-x}$ @C-5 for PMS activation. However, a non-negligible decrease of IOH removal can be observed, which might be caused by the accumulation of IOH and its degradation intermediates on the surface of reactive sites. Interestingly, the IOH removal rate of used  $\text{FeSe}_{2-x}$ @C-5 was recovered to 97.0% after heat regeneration (450 °C). The organic matters on the surface of  $\text{FeSe}_{2-x}$ @C-5 were removed after calcination, resulting in the re-exposure of more active sites. More

importantly, no evident difference in morphology (the size of  $\text{FeSe}_2$  nanoparticles), chemical composition, and microstructure can be observed from the comparison of HRTEM image, XRD pattern, XPS spectra for the fresh and used  $\text{FeSe}_{2-x}$ @C-5 after four cycles (Fig. S15(a–c)). Cyclic voltammetry (CV) measurements (Fig. S15(d)) showed that a well redox capacity is maintained after 100 cycles. All the above results exhibited that the  $\text{FeSe}_{2-x}$ @C-5 had high chemical stability and satisfactory cycle stability, demonstrating that it had brilliant characteristics for potential applications. In addition, the potential application in different actual water matrices was studied for  $\text{FeSe}_{2-x}$ @C-5. River water (Yangtze River) and lake water (Xuanwu Lake) were chosen to simulate the actual water sample and the water quality is listed in Table S4. As described in Fig. 4(d), it could be noticed that an obvious decrease in the degradation rate constant of IOH was observed when deionized water was replaced by river water and lake water. The possible reason for that is the presence of certain level of ions (phosphate and bicarbonate) and natural organic matters in the river water and lake water (Table S4). Nevertheless, the removal rate remained at almost 100% within 30 min, indicating that the potential application of the  $\text{FeSe}_{2-x}$ @C-5/PMS system in low-strength wastewater treatment.

### 3.3. Analysis of the reactive species involved in $\text{FeSe}_{2-x}$ @C-5/PMS system

In PMS-based AOPs,  $\cdot\text{OH}$ ,  $\text{SO}_4^{\cdot-}$ ,  $\text{O}_2^{\cdot-}$ , and  $^1\text{O}_2$  are widely acknowledged possible reactive species inducing pollutant degradation [16,33]. To verify the involved reactive species in the  $\text{FeSe}_{2-x}$ @C-5/PMS system, different free radical quenchers (e.g., methanol for  $\text{SO}_4^{\cdot-}$  and  $\cdot\text{OH}$ , tert-butanol (TBA) for  $\cdot\text{OH}$ , 4-hydroxy-2,2,6,6-tetramethylpiperidine-N-oxyl (TEMPOL) for  $\text{O}_2^{\cdot-}$ , and L-histidine for  $^1\text{O}_2$ ) were utilized to capture the responsive radicals during degradation process [12,55,56]. As depicted in Figs. 5(a) and S16, the reaction rate constant ( $k_{\text{app}}$ ) of IOH without quencher was  $0.1353 \text{ min}^{-1}$  within

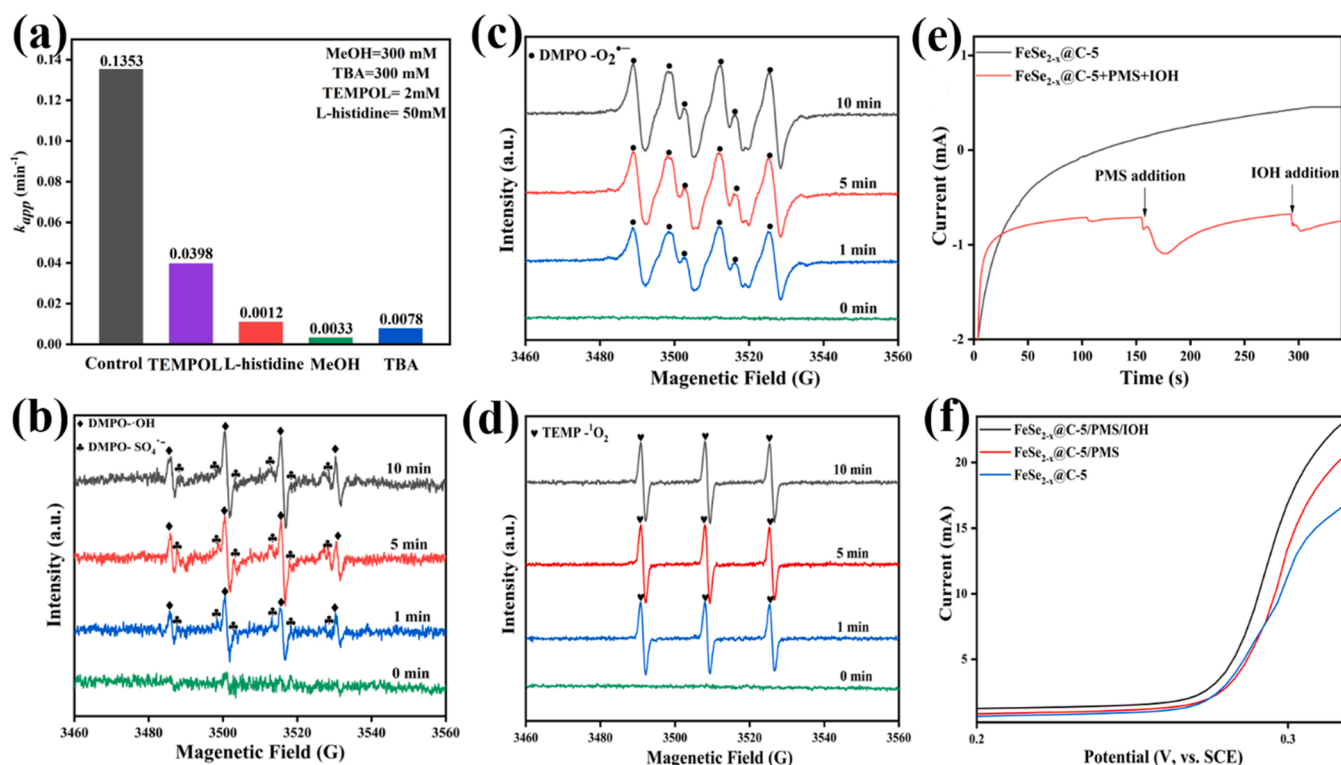


**Fig. 5.** (a) Effects of radical scavengers on IOH removal in  $\text{FeSe}_{2-x}$ @C-5/PMS system. Reaction conditions:  $[\text{IOH}]_0 = 15.0 \text{ mg/L}$ ,  $[\text{PMS}]_0 = 1.5 \text{ mM}$ ,  $[\text{catalyst}]_0 = 0.2 \text{ g/L}$ . The EPR spectra of different reactive species: (b) DMPO- $\cdot\text{OH}$  and DMPO- $\text{SO}_4^{\cdot-}$ , (c) DMPO- $\text{O}_2^{\cdot-}$  and (d) TEMP- $^1\text{O}_2$ . (e) The i-t curves, (f) linear sweep voltammetry (LSV) curves of  $\text{FeSe}_{2-x}$ @C-5,  $\text{FeSe}_{2-x}$ @C-5/PMS, and  $\text{FeSe}_{2-x}$ @C-5/PMS/IOH.



30 min. As MeOH (300 mM) and TBA (300 mM) were added, the reaction rate constant dropped to  $0.0033 \text{ min}^{-1}$  and  $0.0078 \text{ min}^{-1}$ , indicating that the existence of both  $\cdot\text{OH}$  and  $\text{SO}_4^{\bullet-}$  in the  $\text{FeSe}_{2-x}@\text{C-5}/\text{PMS}$  system, with  $\cdot\text{OH}$  exhibiting higher efficiency than  $\text{SO}_4^{\bullet-}$ . Moreover, when 100 mM L-histidine were present, the  $k_{\text{app}}$  declined to  $0.0012 \text{ min}^{-1}$ , revealing that  $^1\text{O}_2$  also played a significant part in IOH degradation. Moreover,  $k_{\text{app}}$  of  $0.0398 \text{ min}^{-1}$  were observed with the presence of 5 mM TEMPOL, demonstrating that  $\text{O}_2^{\bullet-}$  was also dragged in the reaction. Overall, the reactive species including  $\cdot\text{OH}$ ,  $\text{SO}_4^{\bullet-}$ ,  $\text{O}_2^{\bullet-}$ , and  $^1\text{O}_2$  all together contributed to the IOH removal in the  $\text{FeSe}_{2-x}@\text{C-5}/\text{PMS}$  system.

@C-5/PMS system.

*In-situ* electron paramagnetic resonance (EPR) was executed to further probe the presence of reactive species ( $\cdot\text{OH}$ ,  $\text{SO}_4^{\bullet-}$ ,  $\text{O}_2^{\bullet-}$ , and  $^1\text{O}_2$ ). 5,5-dimethyl-1-pyrroline-N-oxide (DMPO) was employed to act as a spin-trapping agent to capture  $\cdot\text{OH}$ ,  $\text{SO}_4^{\bullet-}$  (water solution) and  $\text{O}_2^{\bullet-}$  (methanol medium) [16,33,38]. In addition, 2,2,6,6-tetramethyl-4-piperidine (TEMP) was used to detect  $^1\text{O}_2$  (water medium) [19]. As displayed in Fig. 5(b–d), as expected, no obvious signals were discovered when PMS exists alone, indicating the weak self-decomposition of PMS without catalyst. After  $\text{FeSe}_{2-x}@\text{C-5}$  and PMS were mixed together, the

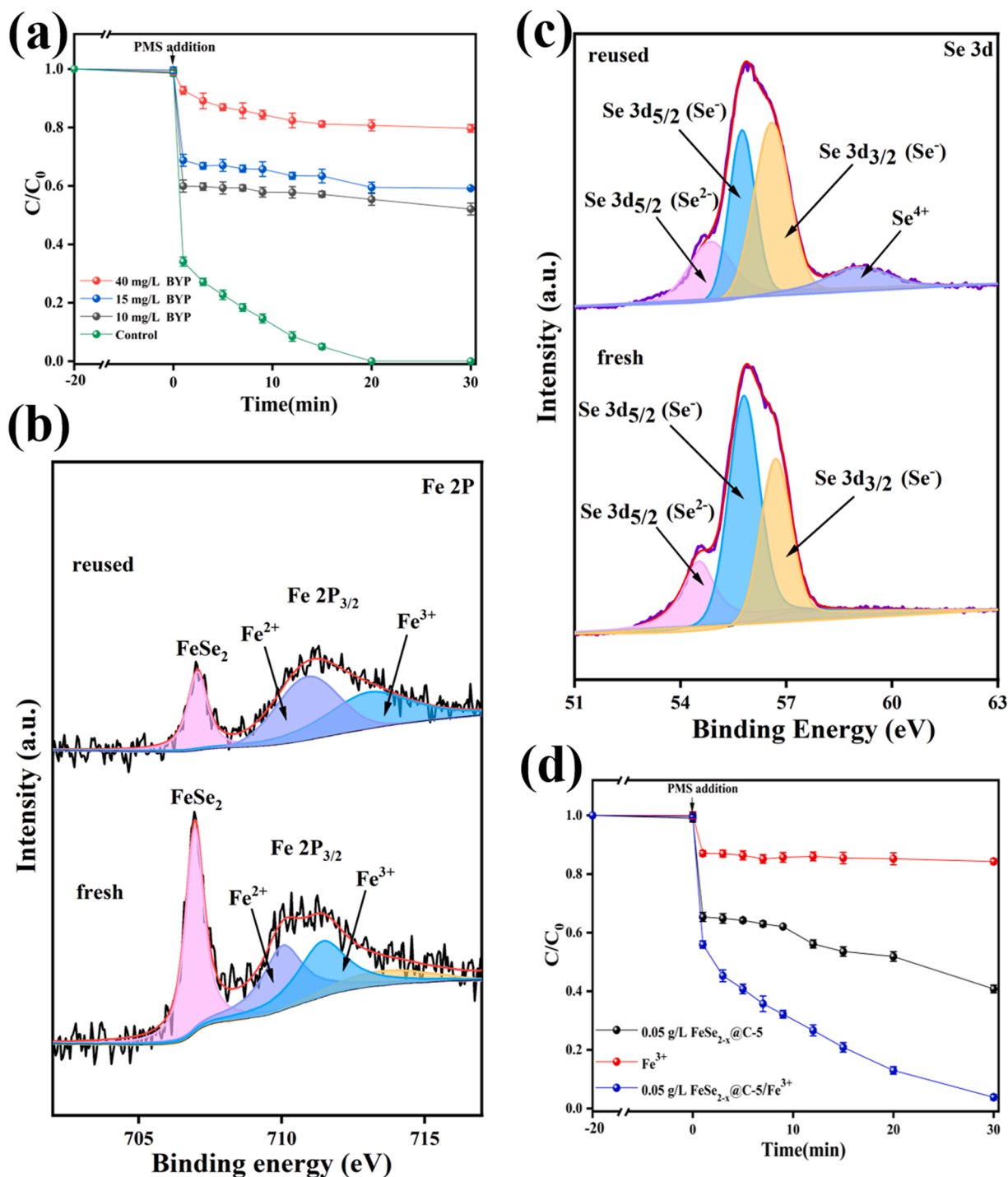


**Fig. 6.** (a) Effects of 2,2-bipyridine (BPY) as a surface  $\text{Fe}^{2+}$  chelator on IOH removal in  $\text{FeSe}_{2-x}@\text{C-5}/\text{PMS}$  system ( $[\text{IOH}]_0 = 15.0 \text{ mg/L}$ ,  $[\text{PMS}]_0 = 1.5 \text{ mM}$ ,  $[\text{catalyst}]_0 = 0.2 \text{ g/L}$ ); (b) XPS analysis of Fe 2p<sub>3/2</sub> and (c) Se 3d for  $\text{FeSe}_{2-x}@\text{C-5}$  before and after reaction; (d) effects of  $\text{Fe}^{3+}$  ion addition on IOH removal in  $\text{FeSe}_{2-x}@\text{C-5}/\text{PMS}$  system ( $[\text{Fe}^{3+}]_0 = 50 \text{ }\mu\text{M}$ ,  $[\text{IOH}]_0 = 15.0 \text{ mg/L}$ ,  $[\text{PMS}]_0 = 1.5 \text{ mM}$ ,  $[\text{catalyst}]_0 = 0.05 \text{ g/L}$ ).

characteristic peaks of DMPO- $\cdot\text{OH}$  (hyperfine splitting constants of  $a_N = a_H = 14.9$  G) with four lines and a weak DMPO- $\text{SO}_4^{\bullet-}$  adducts with six lines (hyperfine splitting constants of  $a_N = 13.2$  G,  $a_H = 9.6$  G,  $a_H = 1.48$  G, and  $a_H = 0.78$  G) were also observed in  $\text{FeSe}_{2-x}$ @C-5/PMS system [36]. The signal of free radicals gradually increases as time elapses (Fig. 5(b)), verifying that  $\text{FeSe}_{2-x}$ @C-5 could activate PMS to generate  $\cdot\text{OH}$  and  $\text{SO}_4^{\bullet-}$  for IOH removal. Furthermore, the six-line characteristic peak of DMPO- $\text{O}_2^{\bullet-}$  and a strong triplet characteristic signal of TEMP- $^1\text{O}_2$  were also captured [33], which verified the existence of  $^1\text{O}_2$  and  $\text{O}_2^{\bullet-}$  in  $\text{FeSe}_{2-x}$ @C-5/PMS system (Fig. 5(c) and (d)). Therefore, the above results are in accordance with the results of the free radical quenching experiments.

Additionally, charge transfer among IOH,  $\text{FeSe}_{2-x}$ @C-5, and PMS was also investigated by electrochemical measurement to further illustrate the nonradical electron-transfer for IOH degradation. As displayed in Fig. 5(e), a small negative current peak could be observed in the i-t curve and the current response increased obviously after the injection of PMS (1 mM) at 156 s, displaying the strong electron transfer between PMS and the surface of  $\text{FeSe}_{2-x}$ @C-5 to form a metastable reactive complex [57]. Besides, an increased current was also observed after adding IOH, suggesting a stable electron transfer between IOH and metastable reactive complex. As expected, the linear sweep voltammetry (LSV) (Fig. 5(f)) further indicated that the charge transfer from IOH to PMS on the carbon surface of  $\text{FeSe}_{2-x}$ @C-5 during the IOH removal process, which was also in consistency with the previous studies [55,56].

### 3.4. The role of Fe and Se species in $\text{FeSe}_{2-x}$ @C-5/PMS system

Theoretically, PMS is activated to generate free radicals by transition metal through single electron transfer process in metal-based heterogeneous catalytic systems [28]. Therefore,  $\text{Fe}^{2+}$  is known as a significant part in the  $\text{FeSe}_{2-x}$ @C-5/PMS system. 2, 2'-bipyridine (BPY), a  $\text{Fe}^{2+}$  complexing agent, was applied to test the direct activation of PMS by  $\text{Fe}^{2+}$  on the surface of  $\text{FeSe}_{2-x}$ @C-5 since BPY can chelate  $\text{Fe}^{2+}$  instead of quenching free radicals (e.g.,  $\text{SO}_4^{\bullet-}$ ,  $\cdot\text{OH}$ , PMS) [58]. As displayed in Fig. 6(a), it shows that BPY could cause a significant inhibitory effect for IOH degradation. As the BPY concentrations rose from 0 to 40 mg/L, the corresponding degradation efficiency of IOH decreased from 100.0% to 19.4% in 30 min. Furthermore, as depicted in the Fe 2p<sub>3/2</sub> spectra in Fig. 6(b), a part of  $\text{Fe}^{2+}$  is transformed into  $\text{Fe}^{3+}$  after reaction, suggesting that redox reaction pathway of the Fe species was related in PMS activation. As expected, the above results demonstrated that  $\text{Fe}^{2+}$  was mainly active centers for the activation of PMS in  $\text{FeSe}_{2-x}$ @C-5/PMS system. In addition, compared with Se 3d spectra of  $\text{FeSe}_{2-x}$ @C-5 before and after reaction (Fig. 6(c)), no signals of  $\text{Se}^{4+}$  can be observed in the Se 3d spectra of fresh  $\text{FeSe}_{2-x}$ @C-5, while a signal of  $\text{Se}^{4+}$  appears in the Se 3d spectra of used  $\text{FeSe}_{2-x}$ @C-5 at 59.1 eV [28], indicating that a small amount of low valence Se species (e.g.,  $\text{Se}^{2-}$ ,  $\text{Se}^-$ ) were oxidized into high valence state during the degradation of IOH. These results indicated that Se species might contribute to the activation of PMS and production of  $\text{Fe}^{2+}$  via electron transfer [28]. To test this hypothesis, commercial ZnSe was chosen as the source of Se species since Zn is thermodynamically stable and cannot activate PMS. As shown in Fig. S17, about 15% of IOH could be removed in ZnSe/PMS system, demonstrating that Se species can provide a small number of electrons for PMS activation and IOH degradation. In addition, to verify that Se species could boost  $\text{Fe}^{2+}$  regeneration,  $\text{Fe}^{3+}$  (50  $\mu\text{M}$ ) ions were added in  $\text{FeSe}_{2-x}$ @C-5/PMS system to evaluate its effects on IOH degradation. Fig. 6(d) exhibited that only 15.7% of IOH can be degraded in  $\text{Fe}^{3+}$ /PMS systems. Meanwhile, low degradation efficiency (59.3%) was also observed in  $\text{FeSe}_{2-x}$ @C-5/PMS system. However, degradation efficiency of IOH reached 96.2% in  $\text{FeSe}_{2-x}$ @C-5/ $\text{Fe}^{3+}$ /PMS system, which was higher than those of  $\text{Fe}^{3+}$ /PMS and  $\text{FeSe}_{2-x}$ @C-5/PMS system. The above results suggested that  $\text{Fe}^{3+}$  can be captured and reduced to  $\text{Fe}^{2+}$  by low valence Se species, enhancing PMS activation and IOH degradation. Furthermore, phenanthroline colorimetry was employed to further verify the

formation of  $\text{Fe}^{2+}$  in the  $\text{FeSe}_{2-x}$ @C-5/ $\text{Fe}^{3+}$  suspension. As depicted in Fig. S18, UV-vis spectroscopy analysis of  $\text{FeSe}_{2-x}$ @C-5/ $\text{Fe}^{3+}$  suspension displayed a significant signal at 510 nm, indicating that  $\text{Fe}^{2+}$  was doubtlessly produced in the  $\text{FeSe}_{2-x}$ @C-5/ $\text{Fe}^{3+}$  system. To further verify the generation of  $\text{Fe}^{2+}$  on the surface of  $\text{FeSe}_{2-x}$ @C-5 particles, the reaction suspension was filtered before the addition of phenanthroline, and no obvious  $\text{Fe}^{2+}$  signals at 510 nm can be observed. The phenomenon demonstrated that free  $\text{Fe}^{3+}$  can be adsorbed on the surface of  $\text{FeSe}_{2-x}$ @C-5 and reduced to  $\text{Fe}^{2+}$ , which might be attributed to the presence of  $\text{V}_{\text{Se}}$ . Overall, the above results indicated that Se species can act as an electron donor to promote the conversion of  $\text{Fe}^{3+}$  to  $\text{Fe}^{2+}$  on the  $\text{FeSe}_{2-x}$ @C-5 surface, and the synergy between Fe and Se species plays a significant part in PMS activation by  $\text{FeSe}_{2-x}$ @C-5.

### 3.5. The role of $\text{V}_{\text{Se}}$ in $\text{FeSe}_{2-x}$ @C-5/PMS system

#### 3.5.1. In-situ Raman monitor

The in-situ Raman experimentation was performed to unveil the interfacial reaction process between catalyst and PMS. As depicted in Fig. 7, three stretching vibration peaks at 1060, 980, and 882  $\text{cm}^{-1}$  were discovered in the pure PMS solution, which were ascribed to the  $-\text{SO}_3$ ,  $\text{SO}_4^{2-}$ , and  $\text{O}-\text{O}$  in  $\text{HSO}_5^-$ , respectively [59]. Hence, the alteration of the intensity for  $-\text{SO}_3$ ,  $\text{SO}_4^{2-}$ , and  $\text{O}-\text{O}$  in  $\text{HSO}_5^-$  were employed to assess the PMS decomposition rate [60]. After the addition of  $\text{FeSe}_{2-x}$ @C-5, it was obvious that the intensity of the three characteristic peaks ( $-\text{SO}_3$ ,  $\text{SO}_4^{2-}$ , and  $\text{O}-\text{O}$  in  $\text{HSO}_5^-$ ) significantly decreased, indicating excellent performance of  $\text{FeSe}_{2-x}$ @C-5 in PMS activation. In addition, a small new peak was detected at 815  $\text{cm}^{-1}$ , which might be attributed to peroxo species (such as a metastable reactive complex) [59], and the result was well consistent with the i-t curve and LSV. Interestingly, compared with  $\text{FeSe}_2$ /PMS,  $\text{FeSe}_{2-x}$ @C-2/PMS, and  $\text{FeSe}_{2-x}$ @C-8/PMS system, it could be clearly observed in  $\text{FeSe}_{2-x}$ @C-5/PMS system that  $\text{O}-\text{O}$  ( $\text{HSO}_5^-$ ) peak intensity was the weakest, which showed a better activation in PMS significantly. As a result, demonstrating that the porous  $\text{FeSe}_{2-x}$ @C-5 with more  $\text{V}_{\text{Se}}$  modification had higher catalytic activity in contrast to  $\text{FeSe}_2$ ,  $\text{FeSe}_{2-x}$ @C-2, and  $\text{FeSe}_{2-x}$ @C-8. In other words,  $\text{V}_{\text{Se}}$  played a significant part in adjusting the activation performance of the catalyst. These results were in agreement with the degradation kinetics of IOH (Fig. 4(b)).

#### 3.5.2. Electrochemical analysis

As evidently unveiled from the above systematic characterization and experimental analysis, the superiority of  $\text{FeSe}_{2-x}$ @C-5 compared with  $\text{FeSe}_{2-x}$ @C-2,  $\text{FeSe}_{2-x}$ @C-8, and  $\text{FeSe}_2$  in PMS activation for IOH

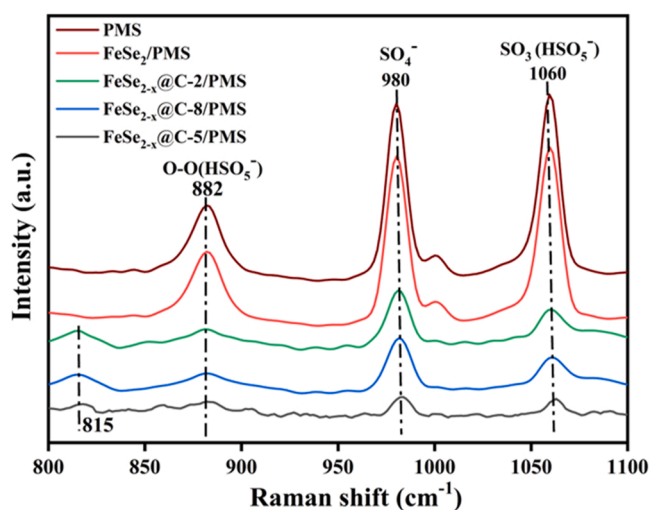


Fig. 7. In-situ Raman spectra for  $\text{FeSe}_2$ /PMS,  $\text{FeSe}_{2-x}$ @C-2/PMS,  $\text{FeSe}_{2-x}$ @C-5/PMS, and  $\text{FeSe}_{2-x}$ @C-8/PMS system.

removal was mainly ascribed to the higher contents of surface  $V_{se}$ . Meanwhile, it is widely acknowledged that defect engineering ( $V_{se}$ ) may effectively adjust the electronic state of the catalyst via regulating local coordination environments of Fe cations [33,37]. To confirm the electronic modulation via  $V_{se}$  in the catalytic reaction, the electrochemical tests were performed to assess the electrical characteristics of catalyst. As illustrated in Mott-Schottky analysis (Fig. 8(a)), the flat band potential ( $E_{FB}$ ) of catalyst was obtained via the intercept. The corresponding  $E_{FB}$  of  $FeSe_2$ ,  $FeSe_{2-x}@C-2$ ,  $FeSe_{2-x}@C-5$ , and  $FeSe_{2-x}@C-8$  is  $-0.22$ ,  $-0.30$ ,  $-0.38$ , and  $-0.42$  V, respectively. In addition, the  $E_{FB}$  indirectly reflects the Fermi level and the feasibility to be an electron donor when catalyst is soaked in reaction medium [61]. As depicted in Fig. 8(b), lower  $E_{FB}$  value represented much higher location of Fermi level, suggesting that  $FeSe_{2-x}@C-5$  was more inclined to provide electrons to trigger the chain reaction towards PMS activation and regulate the interface energetics and reduce reaction barriers for charge transfer. Furthermore, the cyclic voltammetry (CV) curves were also tested to investigate the redox potential of catalyst (Fig. 8(c)). On one hand, the redox area followed the order of  $FeSe_{2-x}@C-5 > FeSe_{2-x}@C-8 > FeSe_{2-x}@C-2 > FeSe_2$ , indicating that the charge storage capacity of  $FeSe_{2-x}@C-5$  was stronger than those of  $FeSe_2$ ,  $FeSe_{2-x}@C-2$ , and  $FeSe_{2-x}@C-8$ . On the other hand, two weak peaks at 0.22 V and 0.32 V in the CV curve of  $FeSe_2$  corresponded to the oxidation potential ( $E^{ox}$ ) and reduction potential ( $E^{red}$ ), demonstrating that the  $Fe^{3+}/Fe^{2+}$

redox reactions were limited on the  $FeSe_2$  with a lower surface  $V_{se}$ . Additionally, compared with the  $FeSe_{2-x}@C-2$  and  $FeSe_{2-x}@C-8$ ,  $FeSe_{2-x}@C-5$  exhibited the higher current intensities at  $E^{ox}$  and  $E^{red}$ , especially at the  $E^{red}$  in the CV curve ( $-5.51$  mA for the  $E^{red}$  and  $9.88$  mA for the  $E^{ox}$ ), implying that the  $Fe^{3+}/Fe^{2+}$  redox reaction on  $FeSe_{2-x}@C-5$  was significantly promoted with more surface  $V_{se}$ . Moreover, the half-wave potential ( $E_{1/2}$ , i.e.,  $[E^{red} + E^{ox}]/2$ ) of  $FeSe_{2-x}@C-5$  was about 0.23 V, which was lower than those of  $FeSe_2$  (0.27 V),  $FeSe_{2-x}@C-2$  (0.26 V), and  $FeSe_{2-x}@C-8$  (0.25 V), demonstrating the easier reduction of  $Fe^{3+}$  to  $Fe^{2+}$  in the  $FeSe_{2-x}@C-5$  system [62]. These results agree well with the generation of  $Fe^{2+}$  during the SR-AOPs (Fig. S19). Besides, the charge transfer in heterogeneous SR-AOPs system were characterized via electrochemical impedance spectroscopy (EIS) (Fig. 8(d)). The semicircle radius followed the order of  $FeSe_{2-x}@C-5 < FeSe_{2-x}@C-8 < FeSe_{2-x}@C-2 < FeSe_2$ , the smaller arc radius indicated a lower charge transfer resistance in  $FeSe_{2-x}@C-5$  [62]. The faster electron transport ability and lower charge transfer resistance of  $FeSe_{2-x}@C-5$  were advantageous for the PMS activation. In conclusion, the above electrochemical test results evidently indicated that the introduction of  $V_{se}$  through defect engineering could not only enhance the charge storage capacity, but also improve the  $Fe^{3+}/Fe^{2+}$  redox cycling of  $FeSe_{2-x}@C-5$  both dynamically (promoting the charge transfer) and thermodynamically (lowering  $Fe^{3+}/Fe^{2+}$  redox potential) aspects. More importantly,  $V_{se}$  can play an important role in ending the

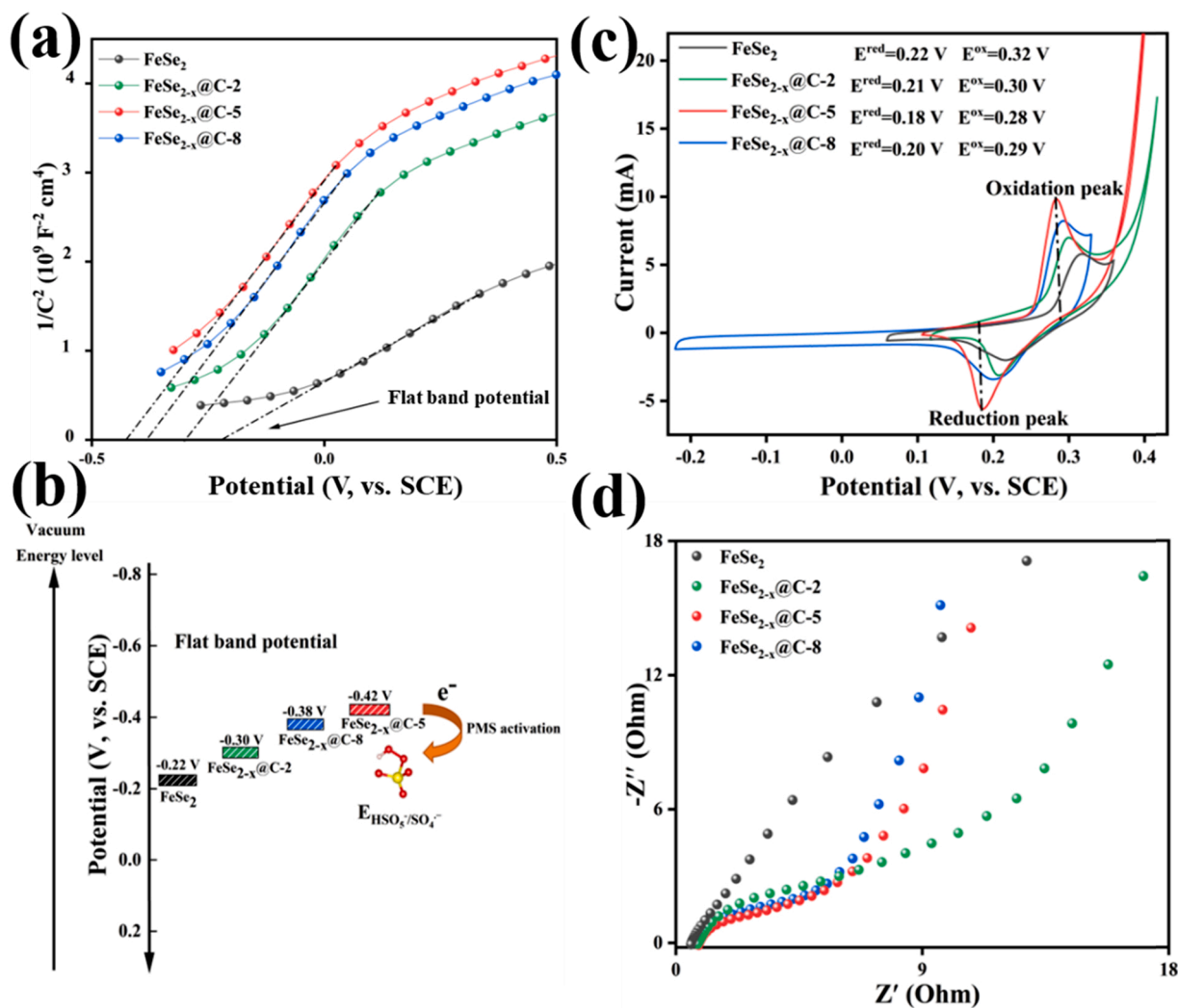


Fig. 8. (a) Mott-Schottky measurements, (b) flat band potential, (c) cyclic voltammetry (CV) measurements and (d) EIS measurements of  $FeSe_2$ ,  $FeSe_{2-x}@C-2$ ,  $FeSe_{2-x}@C-5$  and  $FeSe_{2-x}@C-8$ .



FeSe<sub>2-x</sub>@C-5 with improved electrical conductivity in boosting the charge deliver between the FeSe<sub>2-x</sub>@C-5 and PMS. Consequently, a significantly enhancement in PMS activation was obtained in FeSe<sub>2-x</sub>@C-5/PMS system.

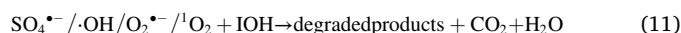
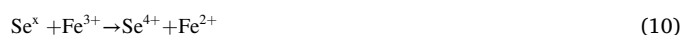
### 3.5.3. Theoretical calculations

DFT computations were further employed to research the importance of V<sub>se</sub> on the catalytic activity enhancement of FeSe<sub>2-x</sub>@C-5. Theoretically, the activation of PMS by catalyst usually follows three steps. Firstly, PMS is quickly adsorbed on the surface of the catalyst. Secondly, the electron is injected into the PMS from catalyst. Finally, the peroxide bond (O–O) of PMS is cracked, generating multiple active radical species (e.g., SO<sub>4</sub><sup>•-</sup>, •OH) [32,33]. In terms of the experimental results, two model surfaces, perfect FeSe<sub>2</sub>@C-5(111) surface without V<sub>se</sub> and the defective FeSe<sub>2-x</sub>@C-5(111) surface with V<sub>se</sub>, were constructed for calculation. The optimized atomic configurations of the perfect FeSe<sub>2</sub>@C-5 (111) and defective FeSe<sub>2-x</sub>@C-5 (111) were shown in Fig. S20(a) and (b). On one hand, from the Bader charge analysis (Fig. 9(a–c)), compared with perfect FeSe<sub>2</sub>@C-5(111), it could be observed that the incorporation of V<sub>se</sub> into FeSe<sub>2-x</sub>@C-5(111) evidently lead to the lower electron distribution of Fe atoms (Fe<sub>23</sub>, Fe<sub>24</sub>). In other words, the defect-engineered (V<sub>se</sub>) catalyst could break the chemical inertness of Fe<sup>3+</sup>/Fe<sup>2+</sup> cycling due to the existence of V<sub>se</sub> and enhance the catalytic performance [26]. Further, the electron properties of these two models were also analyzed employing the densities of states, as portrayed in Fig. 9(d). It could be noticed that the hybridization of Fe 3d–Se 4p played an important part in high density of electrons distributing on the Fermi level for the perfect FeSe<sub>2</sub>@C-5(111) and defective FeSe<sub>2-x</sub>@C-5(111). Besides, the states at Fermi level for defective FeSe<sub>2-x</sub>@C-5(111) (13.2 eV) were much higher than perfect FeSe<sub>2</sub>@C-5(111) (6.3 eV), indicating an enhancement in electron conductivity with the introduction of V<sub>se</sub>. Noticeably, such conductive trait was beneficial to the electronic transportation for PMS activation. Furthermore, Fig. 9(e) and (f) exhibited the optimized geometry of adsorption structure of PMS on the two model surfaces. The adsorption energy of PMS on the catalyst surface (*E<sub>ads</sub>*), electron transfer from catalyst surface to PMS (*Q<sub>et</sub>*), and peroxide bond length of PMS (*l<sub>O-O</sub>*) were computed and displayed in Figs. 9(e) and (f) and S21. Compared with the perfect FeSe<sub>2</sub>@C-5(111)/PMS system, the defective FeSe<sub>2-x</sub>@C-5(111)/PMS system showed larger *E<sub>ads</sub>*, longer *l<sub>O-O</sub>*, and improved charge transfer to PMS, revealing that defective V<sub>se</sub>-rich FeSe<sub>2-x</sub>@C-5(111) was more conducive to the PMS activation to yield active species. Additionally, as shown in the charge density difference analysis (Figs. 9(g), (h) and S22(a), (b)), charge diverts from both the perfect FeSe<sub>2</sub>@C-5(111) and defective FeSe<sub>2-x</sub>@C-5(111) model surfaces to PMS could be observed, implying the chemisorption of PMS on the above two model surfaces. Furthermore, compared with perfect FeSe<sub>2</sub>@C-5(111), the charge density in defective FeSe<sub>2-x</sub>@C-5(111) was promoted, indicating that V<sub>se</sub> can facilitate the enrichment of electrons. Overall, the above theoretical calculations unveiled that the abundant V<sub>se</sub> considerably improve the activation performance of the catalyst towards PMS, which was in accordance with our experimental results.

In summary, in-situ Raman intuitively revealed that V<sub>se</sub> could significantly enhance activation performance of the catalyst for PMS. Further, electrochemical analysis, and DFT calculation results indicated that the introduction of V<sub>se</sub> could improve catalytic activity from the following aspects: (i) enhanced the charge storage capacity and electrical conductivity of FeSe<sub>2-x</sub>@C-5; (ii) improved the Fe<sup>3+</sup>/Fe<sup>2+</sup> redox cycling of FeSe<sub>2-x</sub>@C-5 both dynamically (promoting the charge transfer) and thermodynamically (lowering Fe<sup>3+</sup>/Fe<sup>2+</sup> redox potential); (iii) enlarging *E<sub>ads</sub>*, longer *l<sub>O-O</sub>*, and improved charge transfer to PMS. Overall, V<sub>se</sub> engineering played an important role by subtly modulating the surface electronic state and local coordination environment, leading to a significantly improvement in PMS activation.

### 3.6. The mechanism of reactive species formation in FeSe<sub>2-x</sub>@C-5/PMS system

Based on the results discussed above and previous literature [28,38, 55,60,63,64], a possible PMS activation mechanism and IOH degradation over FeSe<sub>2-x</sub>@C-5 could be described as follows (Fig. 10). Notably, the improved specific surface area and mesoporous structure of FeSe<sub>2-x</sub>@C-5 enhance the molecular diffusion of PMS and IOH. On one hand, PMS (HSO<sub>5</sub><sup>-</sup>) was mainly trapped by the surface V<sub>se</sub> of FeSe<sub>2-x</sub>@C-5 and activated to emancipate a list of active species for IOH degradation. The generation of SO<sub>4</sub><sup>•-</sup> were mainly ascribed to the Fe<sup>2+</sup> over FeSe<sub>2-x</sub>@C-5 surface, which could promote the cleavage for the peroxide bond (O–O) in PMS via one electron transfer reactions (Eq. (2)). The redox cycle could achieve through the reaction between Fe<sup>3+</sup> and HSO<sub>5</sub><sup>-</sup> for continuous generation of radicals (Eq. (3)). Besides, SO<sub>4</sub><sup>•-</sup> could further react with H<sub>2</sub>O to produce •OH (Eq. (4)). Many literatures have proved that oxygen vacancies can reduce O<sub>2</sub> to O<sub>2</sub><sup>•-</sup> [33,38]. Therefore, it was reasonably speculated that the V<sub>se</sub> defects of FeSe<sub>2-x</sub>@C-5 could provide electrons for converting O<sub>2</sub> to O<sub>2</sub><sup>•-</sup> (Eq. (5)) because the physico-chemical properties of V<sub>se</sub> are similar to oxygen vacancies. Furthermore, <sup>1</sup>O<sub>2</sub> could be generated from O<sub>2</sub><sup>•-</sup> (Eqs. (6)–(8)). On the other hand, a stable electron transfer between metastable reactive complex (FeSe<sub>2-x</sub>@C-5-PMS complex) and IOH also existed. Interestingly, Se species could also act as an electron donor to promote PMS activation, although this was not the dominant pathway for radical generation (Eq. (9)). More importantly, Fe<sup>3+</sup> would be reduced by Se species with low valence states (Se<sup>-</sup>, Se<sup>2-</sup>, and SeO<sub>x</sub>) and quickly regenerate Fe<sup>2+</sup> (Eq. (10)). Also, according to the results from the electrochemical tests and DFT calculations, the generated V<sub>se</sub> over FeSe<sub>2-x</sub>@C-5 could not only modulate the surface electronic state of Fe, but also lead to strengthened binding energy (*E<sub>ads</sub>*, *l<sub>O-O</sub>*, and *Q<sub>et</sub>*). As a result, it considerably promoted the activation of PMS. In conclusion, both <sup>1</sup>O<sub>2</sub> and surface electron transport mechanisms occurred as the coupled non-radical pathways in the FeSe<sub>2-x</sub>@C-5/PMS system, which worked together with •OH, SO<sub>4</sub><sup>•-</sup>, and O<sub>2</sub><sup>•-</sup> in efficient degradation of IOH (Eq. (11)).



### 3.7. Degradation pathways of IOH and intermediate product toxicity prediction

To further understand a possible degradation pathway of IOH in FeSe<sub>2-x</sub>@C-5/PMS system. Frontier electron densities (FEDs) calculations were employed to predict the susceptibility of IOH molecule attacked by active free radicals. The optimized structure of IOH, IOH HOMO and IOH LUMO electron orbit were shown in Fig. S23(a–c) and the FEDs values of IOH molecules were listed in Table S5. As illustrated in IOH HOMO picture, the HOMO orbital was principally at benzene

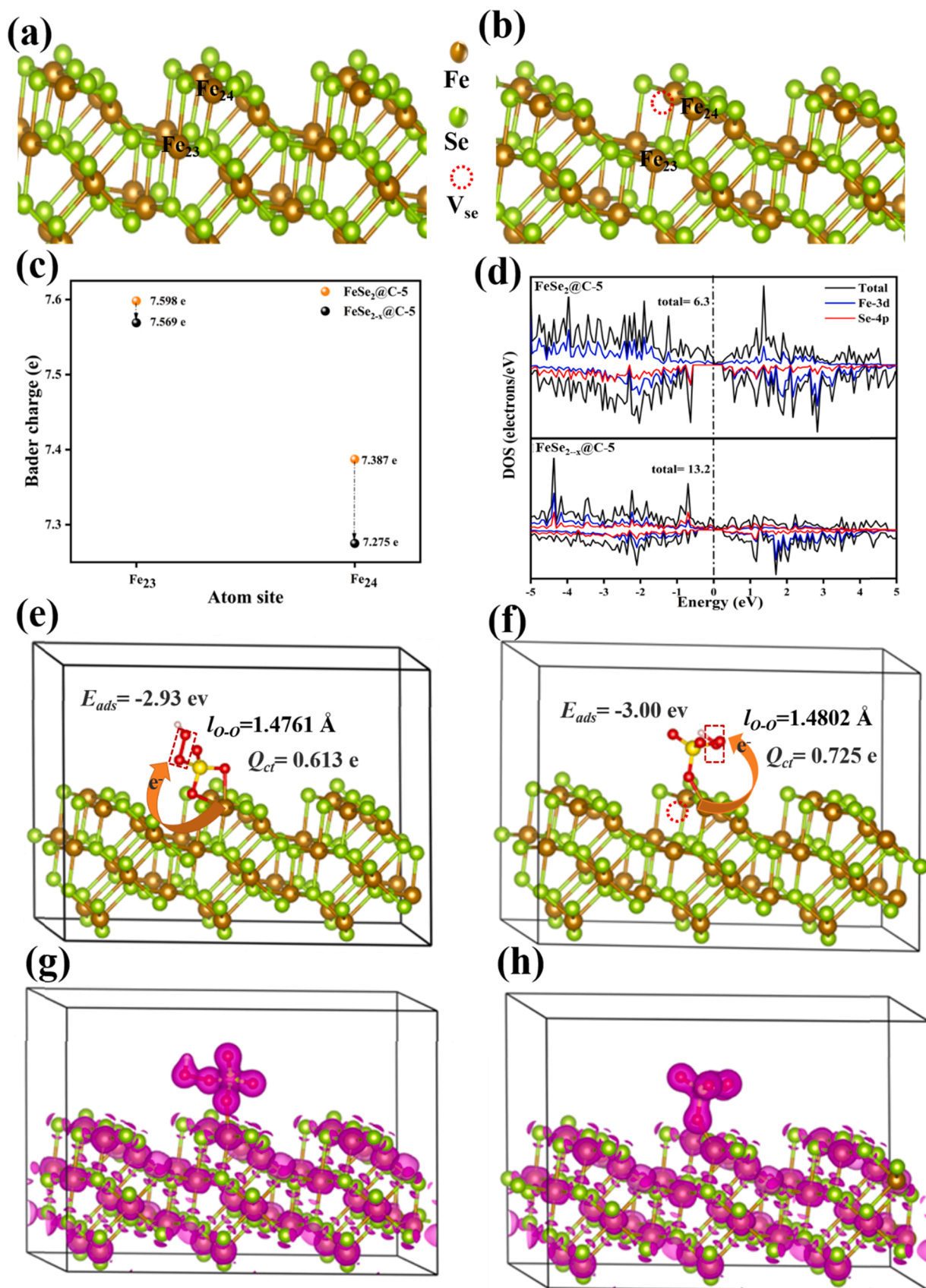


**Fig. 9.** Structure model of (a) FeSe<sub>2</sub> @C-5(111) and (b) FeSe<sub>2-x</sub> @C-5(111); (c) Bader charge analysis of FeSe<sub>2</sub> @C-5(111) and FeSe<sub>2-x</sub> @C-5(111); (d) electron properties of FeSe<sub>2</sub> @C-5(111) and FeSe<sub>2-x</sub> @C-5(111); optimized atomic configurations of the PMS adsorption on (e) FeSe<sub>2</sub> @C-5(111) surface and (f) FeSe<sub>2-x</sub> @C-5(111) surface. charge density difference analysis of the PMS adsorption on (g) FeSe<sub>2</sub> @C-5(111) surface and (h) FeSe<sub>2-x</sub> @C-5(111) surface. (The red, yellow and white spheres represent O, S and H atoms, respectively).

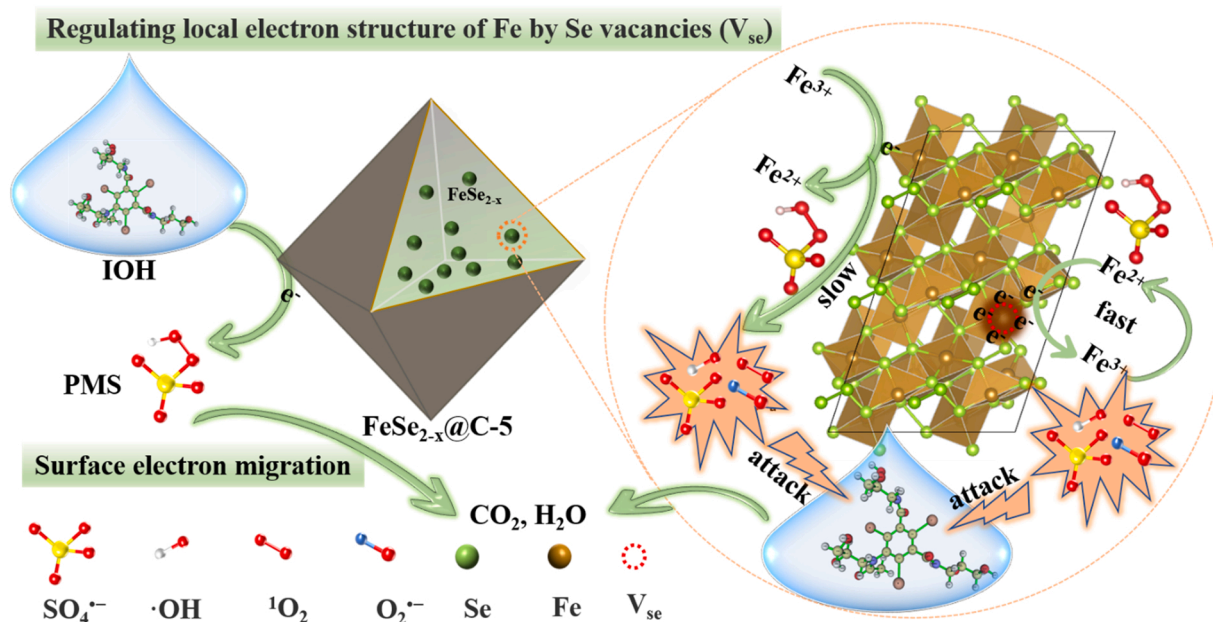


Fig. 10. The possible mechanism of PMS activation for IOH removal in the  $\text{FeSe}_{2-x}\text{@C-5}$ /PMS system.

ring and the iodine atom, which might be attacked by active species. Furthermore, according to the frontier orbital theory, the higher values of  $(\text{FED}_{\text{HOMO}}^2 + \text{FED}_{\text{LUMO}}^2)$  suggested that the atom more inclined to be attacked by free radicals (nucleophilic radicals, electrophilic radicals). However, the higher values of  $2\text{FED}_{\text{HOMO}}^2$  indicated the position tend to be attacked by charge transfer. It was observed that the C1, C3, C5, C6, I7, I8, and I9 exhibited higher  $\text{FED}_{\text{HOMO}}^2 + \text{FED}_{\text{LUMO}}^2$  values, demonstrating that these positions were the most susceptible to be attacked by radical. Moreover, the C4, C6, and I9 displayed higher  $2\text{FED}_{\text{HOMO}}^2$  values, indicating that these sites were expected to suffer preferential attack by charge transfer. The above calculation results are in accordance with previous literature [12,55,56,65].

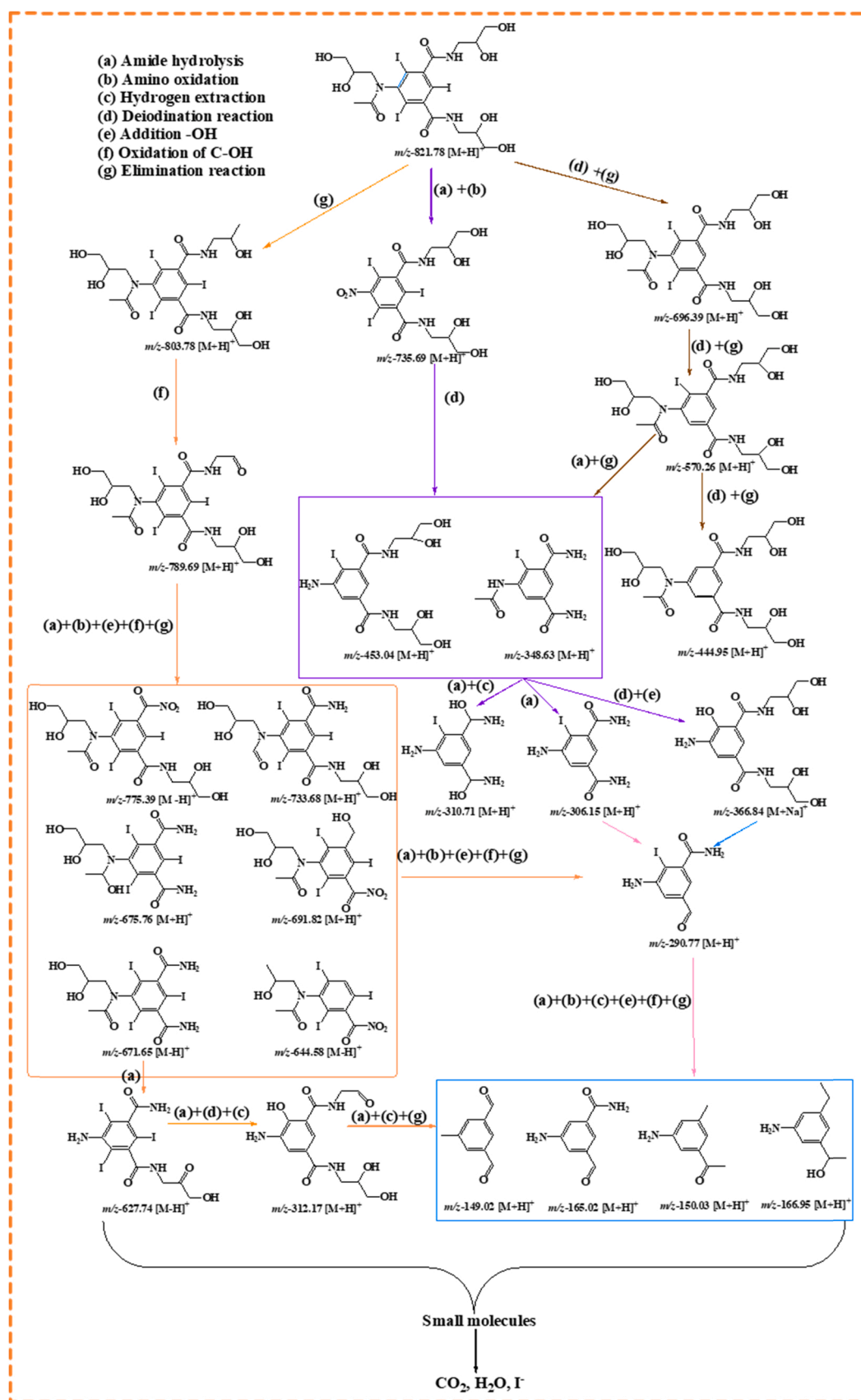
In addition, the LC-MS analyses were employed to discover the possible intermediates during the degradation process of IOH in the  $\text{FeSe}_{2-x}\text{@C-5}$ /PMS system. Twenty-five intermediates could be verified by analysis of structures in combine with literature reports [7,12], and their molecular structures are listed in Table S6 and Fig. S24. The possible pathway was exhibited in Fig. 11, the amide hydrolysis, amine oxidation, hydrogen extraction, deiodination reaction, addition of -OH, oxidation of C-OH, and elimination reaction all played important roles during the degradation process of IOH [7,12,66,67]. At first,  $m/z$ -803.78  $[\text{M}+\text{H}]^+$  was generated by elimination reaction from  $m/z$ -821.78  $[\text{M}+\text{H}]^+$ , meanwhile  $m/z$ -735.69  $[\text{M}+\text{H}]^+$  was formed via the amide hydrolysis and amine oxidation processes. Meanwhile,  $m/z$ -696.39  $[\text{M}+\text{H}]^+$  also could be obtained by losing I7, then I8 and I9 were further attacked to obtain  $m/z$ -444.58  $[\text{M}+\text{H}]^+$ , which was consistent with theoretical calculation.  $m/z$ -789.69  $[\text{M}+\text{H}]^+$  was generated by the oxidation of C-OH from  $m/z$ -803.78  $[\text{M}+\text{H}]^+$ , furthermore,  $m/z$ -789.69  $[\text{M}+\text{H}]^+$  was transformed into  $m/z$ -312.17  $[\text{M}+\text{H}]^+$  and  $m/z$ -291  $[\text{M}+\text{H}]^+$  via a series of reactions. On one hand,  $m/z$ -306  $[\text{M}+\text{H}]^+$ ,  $m/z$ -311  $[\text{M}+\text{H}]^+$ , and  $m/z$ -366.84  $[\text{M}+\text{Na}]^+$  were formed from both  $m/z$ -735.69  $[\text{M}+\text{H}]^+$  and  $m/z$ -570.26  $[\text{M}+\text{H}]^+$  via the amide hydrolysis, deiodination reaction, and elimination reaction. On the other hand, both  $m/z$ -290.77  $[\text{M}+\text{H}]^+$  and  $m/z$ -312.17  $[\text{M}+\text{H}]^+$  were constantly attacked by free and non-free radicals to produce  $m/z$ -149.02  $[\text{M}+\text{H}]^+$ ,  $m/z$ -150.03  $[\text{M}+\text{H}]^+$ ,  $m/z$ -165.02  $[\text{M}+\text{H}]^+$ , and  $m/z$ -166.95  $[\text{M}+\text{H}]^+$ . Finally, as depicted in Fig. S25, 68.5% of the TOC could be removed at 60 min. According to the results of TOC, it could be deduced that some of the small molecules can be eventually mineralized into  $\text{CO}_2$  and  $\text{H}_2\text{O}$ . Moreover, the ECOSAR program was employed to estimate the acute

and chronic toxicity of IOH and its intermediates (Iodinated byproducts) to aquatic organisms such as fish, daphnia and algae (Table S7). As expected, it was obvious that IOH and most identified intermediates (Iodinated byproducts) exhibited no significant biological toxicity to the aquatic organisms. However, there were still some intermediate products showed a high chronic toxicity or acute toxicity to fish, daphnia and algae, including  $m/z$ -644.58  $[\text{M}+\text{H}]^+$ ,  $m/z$ -290.77  $[\text{M}+\text{H}]^+$ ,  $m/z$ -165.02  $[\text{M}+\text{H}]^+$ ,  $m/z$ -150.03  $[\text{M}+\text{H}]^+$ ,  $m/z$ -149.02  $[\text{M}+\text{H}]^+$  and  $m/z$ -166.95  $[\text{M}+\text{H}]^+$ . The above results indicated that during the degradation process of IOH, some toxic intermediates might be generated and pose varied toxicological threats to aquatic organism. In order to reduce ecological risks, the toxic intermediate products of IOH need to be fully removed from the  $\text{FeSe}_{2-x}\text{@C-5}$ /PMS system before being discharged into the natural environment. The extended reaction time or coupled biotechnology were proposed in the future work to accomplish complete mineralization.

#### 4. Conclusion

In summary, a defect-engineered  $\text{V}_{\text{Se}}$ -rich  $\text{FeSe}_{2-x}\text{@C-5}$  with uniform porous carbon-layer coating was prepared via one-step carbonization-selenization process of Fe-MOFs for IOH removal via the activation of PMS. Small  $\text{FeSe}_{2-x}$  nanoparticles can be uniformly wrapped in a porous carbon nanocages, which is beneficial to reduce mass transfer resistance and expose more active sites to accelerate the SR-AOPs reaction. Impressively, the systemic electrochemical measurements and DFT calculations revealed that the defect engineering through  $\text{V}_{\text{Se}}$  incorporation in  $\text{FeSe}_{2-x}\text{@C-5}$  could subtly modulate the surface electronic structure and local coordination environment, from dynamically (promoting charge transfer) and thermodynamically (lowering  $\text{Fe}^{3+}/\text{Fe}^{2+}$  redox potential, enhance adsorption energy, and reduce reaction barriers) aspects, leading to the improvement of PMS activation. Moreover, the EPR, electrochemical tests, and scavenging test indicated that nonradical pathways ( $^1\text{O}_2$ , surface charge migration) work together with radical pathways ( $\cdot\text{OH}$ ,  $\text{SO}_4^{\cdot-}$ ,  $\text{O}_2^{\cdot-}$ ) to promote IOH degradation and mineralization in  $\text{FeSe}_{2-x}\text{@C-5}$ /PMS system. In addition,  $\text{FeSe}_{2-x}\text{@C-5}$ /PMS system exhibited superior stability and adaptability. Accordingly, the findings will not only provide a new design guideline for high performance catalytic materials by structural control integrated defect engineering, but also broaden the range of



Fig. 11. The degradation pathways of IOH in the FeSe<sub>2-x</sub>@C-5/PMS system.

FeSe<sub>2</sub>-based catalysts for extensive environmental applications.

### CRediT authorship contribution statement

**Qiang Zhong:** Conceptualization, Methodology, Investigation, Writing – original draft, Writing – review & editing, Validation, Formal analysis, Visualization, Software. **Chenmin Xu:** Writing – review & editing, Funding acquisition. **Yazi Liu:** Writing – review & editing. **Qiuyi Ji:** Writing – review & editing. **Zhe Xu:** Writing – review & editing. **Dunyu Sun:** Data curation. **Shuohua Zhou:** Data curation. **Bing Yang:** Data curation. **Yinhao Dai:** Data curation. **Chengdu Qi:** Data curation. **Shaogui Yang:** Resources, Writing – review & editing, Funding acquisition. **Huan He:** Resources, Writing – review & editing, Funding acquisition. **Shiyan Li:** Writing – review & editing. **Cheng Sun:** Writing – review & editing.

### Declaration of Competing Interest

There are no conflicts to declare.

### Acknowledgments

This work was supported by the Natural Science Foundation of Jiangsu Province, China (Nos. BK20200721 and BK20190718), the National Natural Science Foundation of China Youth Science Foundation Project (No. 51908293), the Natural Science Foundation of the Higher Education Institutions of Jiangsu Province, China (No. 19KJB610016), the National Natural Science Foundation of China (No. 21777067), the Six Talent Peaks Project in Jiangsu Province, China (No. JNHB-105), the Primary Research & Development Plan of Jiangsu Province, China (No. BE2019743), and the Postgraduate Research & Practice Innovation Program of Jiangsu Province (No. KYCX21\_1399).

### Appendix A. Supplementary material

Supplementary data associated with this article can be found in the online version at [doi:10.1016/j.apcatb.2022.121259](https://doi.org/10.1016/j.apcatb.2022.121259).

### References

- [1] M.K. Abd El-Rahman, S.M. Riad, S.A.A. Gawad, E.M. Fawaz, M.A. Shehata, Stability indicating spectrophotometric and spectrodensitometric methods for the determination of diatrizoate sodium in presence of its degradation product, *Spectrochim. Acta Part A Mol. Biomol. Spectrosc.* 136 (2015) 1167–1174.
- [2] C. Christiansen, X-ray contrast media - an overview, *Toxicology* 209 (2005) 185–187.
- [3] T. Anumol, A. Vijayanandan, M. Park, L. Philip, S.A. Snyder, Occurrence and fate of emerging trace organic chemicals in wastewater plants in Chennai, India, *Environ. Int.* 92–93 (2016) 33–42.
- [4] J.L. Kormos, M. Schulz, T.A. Ternes, Occurrence of iodinated X-ray contrast media and their biotransformation products in the urban water cycle, *Environ. Sci. Technol.* 45 (2011) 8723–8732.
- [5] K. Noedler, T. Licha, K. Bester, M. Sauter, Development of a multi-residue analytical method, based on liquid chromatography-tandem mass spectrometry, for the simultaneous determination of 46 micro-contaminants in aqueous samples, *J. Chromatogr. A* 1217 (2010) 6511–6521.
- [6] B. Zonja, A. Delgado, S. Perez, D. Barcelo, LC-HRMS Suspect screening for detection-based prioritization of iodinated contrast media photodegradates in surface waters, *Environ. Sci. Technol.* 49 (2015) 3464–3472.
- [7] H. He, W. Wang, C. Xu, S. Yang, C. Sun, X. Wang, Y. Yao, N. Mi, W. Xiang, S. Li, G. Liu, Highly efficient degradation of iohexol on a heterostructured graphene-analogue boron nitride coupled Bi<sub>2</sub>MoO<sub>6</sub> photocatalyst under simulated sunlight, *Sci. Total Environ.* 730 (2020), 139100.
- [8] M.E. Gale, A.H. Robbins, R.J. Hamburger, W.C. Widrich, Renal toxicity of contrast agents: iopamidol, iothalamate, and diatrizoate, *AJR Am. J. Roentgenol.* 142 (1984) 333–335.
- [9] W. Gartner, M. Weissel, Do iodine-containing contrast media induce clinically relevant changes in thyroid function parameters of euthyroid patients within the first week? *Thyroid* 14 (2004) 521–524.
- [10] S.E. Duirk, C. Lindell, C.C. Cornelison, J. Kormos, T.A. Ternes, M. Attene-Ramos, J. Osoli, E.D. Wagner, M.J. Plewa, S.D. Richardson, Formation of toxic iodinated disinfection by-products from compounds used in medical imaging, *Environ. Sci. Technol.* 45 (2011) 6845–6854.
- [11] C. Hu, Y. Du, Y. Lin, S. Hua, Y. Hou, Y. Deng, J. Zhang, S. Ren, C. Dong, C. Chen, C. Wu, Kinetics of iohexol degradation by ozonation and formation of DBPs during post-chlorination, *J. Water Process Eng.* 35 (2020), 101200.
- [12] W. Xiang, Q. Ji, C. Xu, Y. Guo, Y. Liu, D. Sun, W. Zhou, Z. Xu, C. Qi, S. Yang, S. Li, C. Sun, H. He, Accelerated photocatalytic degradation of iohexol over Co<sub>3</sub>O<sub>4</sub>/g-C<sub>3</sub>N<sub>4</sub>/Bi<sub>2</sub>O<sub>2</sub>CO<sub>3</sub> of p-n/n-n dual heterojunction under simulated sunlight by persulfate, *Appl. Catal. B Environ.* 285 (2021), 119847.
- [13] D. Sun, J. Mao, L. Cheng, X. Yang, H. Li, L. Zhang, W. Zhang, Q. Zhang, P. Li, Magnetic g-C<sub>3</sub>N<sub>4</sub>/NiFe<sub>2</sub>O<sub>4</sub> composite with enhanced activity on photocatalytic disinfection of aspergillus flavus, *Chem. Eng. J.* 418 (2021), 129417.
- [14] Y. Liu, X. Wang, F. Tian, H. Xing, R. Chen, Y. Shen, Degradation of iohexol by UV irradiation: kinetics, pathways and iodinated trihalomethanes formation during post-chlorination, *Desalin. Water Treat.* 83 (2017) 56–65.
- [15] A. Haiss, K. Kummerer, Biodegradability of the X-ray contrast compound diatrizoic acid, identification of aerobic degradation products and effects against sewage sludge micro-organisms, *Chemosphere* 62 (2006) 294–302.
- [16] S. Giannakis, K. Lin, F. Ghanbari, A review of the recent advances on the treatment of industrial wastewaters by sulfate radical-based advanced oxidation processes (SR-AOPs), *Chem. Eng. J.* 406 (2021), 127083.
- [17] L. Gan, Q. Zhong, A. Geng, L. Wang, C. Song, S. Han, J. Cui, L. Xu, Cellulose derived carbon nanofiber: a promising biochar support to enhance the catalytic performance of CoFe<sub>2</sub>O<sub>4</sub> in activating peroxymonosulfate for recycled dimethyl phthalate degradation, *Sci. Total Environ.* 694 (2019), 133705.
- [18] C. Hu, Y. Hou, Y. Lin, Y. Deng, S. Hua, Y. Du, C. Chen, C. Wu, Investigation of iohexol degradation kinetics by using heat-activated persulfate, *Chem. Eng. J.* 379 (2019), 122403.
- [19] P. Duan, Y. Qi, S. Feng, X. Peng, W. Wang, Y. Yue, Y. Shang, Y. Li, B. Gao, X. Xu, Enhanced degradation of clothianidin in peroxymonosulfate/catalyst system via core-shell FeMn @ N-C and phosphate surrounding, *Appl. Catal. B Environ.* 267 (2020), 118717.
- [20] R. Ding, W. Li, C. He, Y. Wang, X. Liu, G. Zhou, Y. Mu, Oxygen vacancy on hollow sphere CuFe<sub>2</sub>O<sub>4</sub> as an efficient Fenton-like catalysis for organic pollutant degradation over a wide pH range, *Appl. Catal. B Environ.* 291 (2021), 120069.
- [21] Y. Yao, H. Chen, C. Lian, F. Wei, D. Zhang, G. Wu, B. Chen, S. Wang, Fe, Co, Ni nanocrystals encapsulated in nitrogen-doped carbon nanotubes as Fenton-like catalysts for organic pollutant removal, *J. Hazard. Mater.* 314 (2016) 129–139.
- [22] H. Zhou, H. Zhang, Y. He, B. Huang, C. Zhou, G. Yao, B. Lai, Critical review of reductant-enhanced peroxide activation processes: Trade-off between accelerated Fe<sup>3+</sup>/Fe<sup>2+</sup> cycle and quenching reactions, *Appl. Catal. B Environ.* 286 (2021), 119900.
- [23] G. Zhao, J. Zou, X. Chen, L. Liu, Y. Wang, S. Zhou, X. Long, J. Yu, F. Jiao, Iron-based catalysts for persulfate-based advanced oxidation process: microstructure, property and tailoring, *Chem. Eng. J.* 421 (2020), 127845.
- [24] I.A. Ike, K.G. Linden, J.D. Orbell, M. Duke, Critical review of the science and sustainability of persulfate advanced oxidation processes, *Chem. Eng. J.* 338 (2018) 651–669.
- [25] S. Navalon, M. de Miguel, R. Martin, M. Alvaro, H. Garcia, Enhancement of the catalytic activity of supported gold nanoparticles for the Fenton reaction by light, *J. Am. Chem. Soc.* 133 (2011) 2218–2226.
- [26] L. Zhang, C. Lu, F. Ye, R. Pang, Y. Liu, Z. Wu, Z. Shao, Z. Sun, L. Hu, Selenic acid etching assisted vacancy engineering for designing highly active electrocatalysts toward the oxygen evolution reaction, *Adv. Mater.* 33 (2021), 2007523.
- [27] Q. Pan, M. Zhang, L. Zhang, Y. Li, Y. Li, C. Tan, F. Zheng, Y. Huang, H. Wang, Q. Li, FeSe<sub>2</sub>@C microrods as a superior long-life and high-rate anode for sodium ion batteries, *ACS Nano* 14 (2020) 17683–17692.
- [28] G. Fang, T. Zhang, H. Cui, D.D. Dionysiou, C. Liu, J. Gao, Y. Wang, D. Zhou, Synergy between iron and selenide on FeSe<sub>2</sub>(111) surface driving peroxymonosulfate activation for efficient degradation of pollutants, *Environ. Sci. Technol.* 54 (2020) 15489–15498.
- [29] G.R. Cai, W. Zhang, L. Jiao, S.H. Yu, H.L. Jiang, Template-directed growth of well-aligned MOF arrays and derived self-supporting electrodes for water splitting, *Chem* 2 (2017) 791–802.
- [30] J. Liu, S.J. Hou, W.J. Li, A.S. Bandarenka, R.A. Fischer, Recent approaches to design electrocatalysts based on metal-organic frameworks and their derivatives, *Chem. Asian J.* 14 (2019) 3474–3501.
- [31] H. Hong, J. Liu, H. Huang, C.A. Etogo, X. Yang, B. Guan, L. Zhang, Ordered macro-porous metal-organic framework single crystals and their Derivatives for rechargeable aluminum-ion batteries, *J. Am. Chem. Soc.* 141 (2019) 14764–14771.
- [32] M. Zhang, C. Xiao, X. Yan, S. Chen, C. Wang, R. Luo, J. Qi, X. Sun, L. Wang, J. Li, Efficient removal of organic pollutants by metal-organic framework derived Co/C yolk-shell nanoreactors: size-exclusion and confinement effect, *Environ. Sci. Technol.* 54 (2020) 10289–10300.
- [33] P. Li, Y. Lin, S. Zhao, Y. Fu, W. Li, R. Chen, S. Tian, Defect-engineered Co<sub>3</sub>O<sub>4</sub> with porous multishelled hollow architecture enables boosted advanced oxidation processes, *Appl. Catal. B Environ.* 298 (2021), 120596.
- [34] W. Xu, W. Xue, H. Huang, J. Wang, C. Zhong, D. Mei, Morphology controlled synthesis of α-Fe<sub>2</sub>O<sub>3-x</sub> with benzimidazole-modified Fe-MOFs for enhanced photo-Fenton-like catalysis, *Appl. Catal. B Environ.* 291 (2021), 120129.
- [35] W. Li, X. Wu, S. Li, W. Tang, Y. Chen, Magnetic porous Fe<sub>3</sub>O<sub>4</sub>/carbon octahedra derived from iron-based metal-organic framework as heterogeneous Fenton-like catalyst, *Appl. Surf. Sci.* 436 (2018) 252–262.
- [36] M. Pu, J. Wan, F. Zhang, M.L. Brusseau, D. Ye, J. Niu, Insight into degradation mechanism of sulfamethoxazole by metal-organic framework derived novel magnetic Fe@C composite activated persulfate, *J. Hazard. Mater.* 414 (2021), 125598.

- [37] L. Su, P. Wang, X. Ma, J. Wang, S. Zhan, Regulating local electron density of iron single sites by introducing nitrogen vacancies for efficient photo-Fenton process, *Angew. Chem.* 133 (2021) 21431–21436.
- [38] S. Guo, H. Wang, W. Yang, H. Fida, L. You, K. Zhou, Scalable synthesis of Ca-doped  $\alpha$ -Fe<sub>2</sub>O<sub>3</sub> with abundant oxygen vacancies for enhanced degradation of organic pollutants through peroxymonosulfate activation, *Appl. Catal. B Environ.* 262 (2020), 118250.
- [39] F. Lai, W. Zong, G. He, Y. Xu, H. Huang, B. Weng, D. Rao, J.A. Martens, J. Hofkens, I.P. Parkin, T. Liu, N<sub>2</sub> electroreduction to NH<sub>3</sub> by selenium vacancy-rich ReSe<sub>2</sub> catalysis at an abrupt interface, *Angew. Chem.* 59 (2020) 13320–13327.
- [40] M. Zhao, K. Yuan, Y. Wang, G. Li, J. Guo, L. Gu, W. Hu, H. Zhao, Z. Tang, Metal-organic frameworks as selectivity regulators for hydrogenation reactions, *Nature* 539 (2016) 76–80.
- [41] K. Bu, B. Wang, W. Zhang, Y. Fei, Y. Zheng, F. Ai, Z. Wu, Q. Wang, H. Wo, J. Zhao, C. Jin, Y. Yin, Study of intrinsic defect states of FeSe with scanning tunneling microscopy, *Phys. Rev. B* 100 (2019), 134502.
- [42] X. Mao, J.-G. Kim, J. Han, H.S. Jung, S.G. Lee, N.A. Kotov, J. Lee, Phase-pure FeSe<sub>x</sub> (x=1, 2) nanoparticles with one-and two-photon luminescence, *J. Am. Chem. Soc.* 136 (2014) 7189–7192.
- [43] K. Karuppasamy, P. Santhoshkumar, T. Hussain, D. Vikraman, C. Yim, S. Hussain, P. Shanmugam, A. Alfanzati, S. Manickam, H. Kim, Influence of selenium precursors on the formation of iron selenide nanostructures (FeSe<sub>2</sub>): efficient electro-Fenton catalysts for detoxification of harmful organic dyestuffs, *Chemosphere* 272 (2021), 129639.
- [44] M. Yousaf, Z. Wang, Y. Wang, Y. Chen, U. Ali, M. Maqbool, A. Imran, N. Mahmood, P. Gao, R.P.S. Han, Core-shell FeSe<sub>2</sub>/C nanostructures embedded in a carbon framework as a free standing anode for a sodium ion battery, *Small* 16 (2020), 2002200.
- [45] E. Bastola, K.P. Bhandari, A.J. Matthews, N. Shrestha, R.J. Ellingson, Elemental anion thermal injection synthesis of nanocrystalline marcasite iron dichalcogenide FeSe<sub>2</sub> and FeTe<sub>2</sub>, *RSC Adv.* 6 (2016) 69708–69714.
- [46] C.E.M. Campos, J.C. de Lima, T.A. Grandi, K.D. Machado, V. Drago, P.S. Pizani, XRD, DSC, MS and RS studies of Fe<sub>75</sub>Se<sub>25</sub> iron selenide prepared by mechano-synthesis, *J. Magn. Magn. Mater.* 270 (2004) 89–98.
- [47] Y. Sun, J. Meng, H.X. Ju, J.F. Zhu, Q.X. Li, Q. Yang, Electrochemical activity of 1T structured rhenium selenide nanosheets via electronic structural modulation from selenium-vacancy generation, *J. Mater. Chem. A* 6 (2018) 22526–22533.
- [48] P. Ge, H. Hou, S. Li, L. Yang, X. Ji, Tailoring rod-like FeSe<sub>2</sub> coated with nitrogen-doped carbon for high-performance sodium storage, *Adv. Funct. Mater.* 28 (2018), 1801765.
- [49] H.N. He, D. Huang, Q.M. Gan, J.N. Hao, S.L. Liu, Z.B. Wu, W.K. Pang, B. Johannessen, Y.G. Tang, J.L. Luo, H.Y. Wang, Z.P. Guo, Anion vacancies regulating endows MoSSe with fast and stable potassium ion storage, *ACS Nano* 13 (2019) 11843–11852.
- [50] M. Wang, Z. Sun, H. Ci, Z. Shi, L. Shen, C. Wei, Y. Ding, X. Yang, J. Sun, Identifying the evolution of Se-vacancy-modulated MoSe<sub>2</sub> pre-catalyst in Li-S chemistry, *Angew. Chem.* 60 (2021) 24558–24565.
- [51] Z. Wang, B. Wen, Q. Hao, L. Liu, C. Zhou, X. Mao, X. Lang, W. Yin, D. Dai, A. Selloni, X. Yang, Localized excitation of Ti<sup>3+</sup> ions in the photoabsorption and photocatalytic activity of reduced rutile TiO<sub>2</sub>, *J. Am. Chem. Soc.* 137 (2015) 9146–9152.
- [52] X. Fang, L. Gan, L. Wang, H. Gong, L. Xu, Y. Wu, H. Lu, S. Han, J. Cui, C. Xia, Enhanced degradation of bisphenol A by mixed ZIF derived CoZn oxide encapsulated N-doped carbon via peroxymonosulfate activation: the importance of N doping amount, *J. Hazard. Mater.* 419 (2021), 126363–126363.
- [53] M. Thommes, K. Kaneko, A.V. Neimark, J.P. Olivier, F. Rodríguez-Reinoso, J. Rouquerol, K.S.W. Sing, Physisorption of gases, with special reference to the evaluation of surface area and pore size distribution (IUPAC technical report), *Pure Appl. Chem.* 87 (2015) 1051–1069.
- [54] S. Ye, G. Zeng, X. Tan, H. Wu, J. Liang, B. Song, N. Tang, P. Zhang, Y. Yang, Q. Chen, X. Li, Nitrogen-doped biochar fiber with graphitization from Boehmeria nivea for promoted peroxymonosulfate activation and non-radical degradation pathways with enhancing electron transfer, *Appl. Catal. B Environ.* 269 (2020), 118850.
- [55] W. Du, Q. Zhang, Y. Shang, W. Wang, Q. Li, Q. Yue, B. Gao, X. Xu, Sulfate saturated biosorbent-derived Co-S@NC nanoarchitecture as an efficient catalyst for peroxymonosulfate activation, *Appl. Catal. B Environ.* 262 (2020), 118302.
- [56] C. Chen, T. Ma, Y. Shang, B. Gao, B. Jin, H. Dan, Q. Li, Q. Yue, Y. Li, Y. Wang, X. Xu, In-situ pyrolysis of enteromorpha as carbocatalyst for catalytic removal of organic contaminants: considering the intrinsic N/Fe in enteromorpha and non-radical reaction, *Appl. Catal. B Environ.* 250 (2019) 382–395.
- [57] M. Wang, Y. Cui, H. Cao, P. Wei, C. Chen, X. Li, J. Xu, G. Sheng, Activating peroxydisulfate with Co<sub>3</sub>O<sub>4</sub>/NiCo<sub>2</sub>O<sub>4</sub> double-shelled nanocages to selectively degrade bisphenol A - a nonradical oxidation process, *Appl. Catal. B Environ.* 282 (2021), 119585.
- [58] Y. Ren, M. Shi, W. Zhang, D.D. Dionysiou, J. Lu, C. Shan, Y. Zhang, L. Lv, B. Pan, Enhancing the Fenton-like catalytic activity of nFe<sub>2</sub>O<sub>3</sub> by MIL-53(Cu) support: a mechanistic investigation, *Environ. Sci. Technol.* 54 (2020) 5258–5267.
- [59] K. Qian, H. Chen, W. Li, Z. Ao, Y. Wu, X. Guan, Single-Atom Fe catalyst outperforms its homogeneous counterpart for activating peroxymonosulfate to achieve effective degradation of organic contaminants, *Environ. Sci. Technol.* 55 (2021) 7034–7043.
- [60] Y. Chen, G. Zhang, H. Liu, J. Qu, Confining free radicals in close vicinity to contaminants enables ultrafast Fenton-like processes in the interspacing of MoS<sub>2</sub> membranes, *Angew. Chem.* 58 (2019) 8134–8138.
- [61] Z. Xu, Y. Wu, Q. Ji, T. Li, C. Xu, C. Qi, H. He, S. Yang, S. Li, S. Yan, C. Sun, L. Zhang, Z. Zou, Understanding spatial effects of tetrahedral and octahedral cobalt cations on peroxymonosulfate activation for efficient pollution degradation, *Appl. Catal. B Environ.* 291 (2021), 120072.
- [62] T. Li, Y. Chen, X. Wang, J. Liang, L. Zhou, Modifying organic carbon in Fe<sub>3</sub>O<sub>4</sub>-loaded schwertmannite to improve heterogeneous Fenton activity through accelerating Fe(II) generation, *Appl. Catal. B Environ.* 285 (2021), 119830.
- [63] H. Chen, Y. Xu, K. Zhu, H. Zhang, Understanding oxygen-deficient La<sub>2</sub>CuO<sub>4</sub>-delta perovskite activated peroxymonosulfate for bisphenol A degradation: the role of localized electron within oxygen vacancy, *Appl. Catal. B Environ.* 284 (2021), 119732.
- [64] H. Zhang, C. Li, L. Lyu, C. Hu, Surface oxygen vacancy inducing peroxymonosulfate activation through electron donation of pollutants over cobalt-zinc ferrite for water purification, *Appl. Catal. B Environ.* 270 (2020), 118874.
- [65] X. Long, C. Feng, D. Ding, N. Chen, S. Yang, H. Chen, X. Wang, R. Chen, Oxygen vacancies-enriched CoFe<sub>2</sub>O<sub>4</sub> for peroxymonosulfate activation: the reactivity between radical-nonradical coupling way and bisphenol A, *J. Hazard. Mater.* 418 (2021), 126357.
- [66] C.L. Eversloh, N. Henning, M. Schulz, T.A. Ternes, Electrochemical treatment of iopromide under conditions of reverse osmosis concentrates - elucidation of the degradation pathway, *Water Res.* 48 (2014) 237–246.
- [67] L. Zhou, C. Ferronato, J.-M. Chovelon, M. Sleiman, C. Richard, Investigations of diatrizoate degradation by photo-activated persulfate, *Chem. Eng. J.* 311 (2017) 28–36.